JOURNAL OF PETROLOGY | VOLUME 53 | NUMBER 7 | PAGES 1417–1448 | 2012 | doi:10.1093/petrology/egs021

# Chronology and Geochemistry of Lavas from the Nazca Ridge and Easter Seamount Chain: an ~30 Myr Hotspot Record

**JYOTIRANJAN S. RAY[1,2]*, JOHN J. MAHONEY[2], ROBERT A. DUNCAN[3], JYOTISANKAR RAY[2,4], PAUL WESSEL[2] AND DAVID F. NAAR[5]**

[1]PHYSICAL RESEARCH LABORATORY, NAVRANGPURA, AHMEDABAD 380009, INDIA

[2]SCHOOL OF OCEAN AND EARTH SCIENCE AND TECHNOLOGY, UNIVERSITY OF HAWAII, HONOLULU, HI 96822, USA

[3]COLLEGE OF OCEANIC AND ATMOSPHERIC SCIENCES, OREGON STATE UNIVERSITY, CORVALLIS, OR 97331, USA

[4]DEPARTMENT OF GEOLOGY, UNIVERSITY OF CALCUTTA, KOLKATA 700019, INDIA

[5]COLLEGE OF MARINE SCIENCE, UNIVERSITY OF SOUTH FLORIDA, ST. PETERSBURG, FL 33701, USA

**RECEIVED FEBRUARY 25, 2011; ACCEPTED FEBRUARY 22, 2012**
**ADVANCE ACCESS PUBLICATION APRIL 11, 2012**

*The Easter Seamount Chain and Nazca Ridge are two of the most conspicuous volcanic features on the Nazca plate. Many questions about their nature and origin have remained unresolved because of a lack of geochronological and geochemical data for large portions of both chains. New $^{40}Ar-^{39}Ar$ incremental heating age determinations for dredged rocks from volcanoes east of Salas y Gomez Island show that, with very few exceptions, ages increase steadily to the east from 1·4 to 30 Ma, confirming that the two chains are parts of the same hotspot trail and indicating a hotspot location near Salas y Gomez rather than beneath Easter Island some 400 km farther west. Most of the volcanoes appear to have been erupted onto seafloor that was 5–13 Myr old, and no systematic variation in seafloor age at the time of seamount formation is apparent. At about 23 Ma, the formation of the Nazca Ridge ceased and that of the Easter Seamount Chain began, corresponding to a change in the direction of motion of the Nazca plate. Most of the studied rocks are moderately alkalic to transitional basalts. Their geochemical characteristics suggest that they represent relatively small mean amounts of partial melting initiating in garnet-bearing mantle and ending in the spinel facies. Nd–Sr–Pb isotopic compositions are within the range of values previously observed for volcanoes of the Easter Seamount Chain, west of Easter Island; moreover, most of our data cluster in a rather small part of this range [e.g. $\varepsilon_{Nd}(t)$ is between +6·0 and +4·0]. The results indicate that the mantle source has consisted of the same two principal components, a C/FOZO-type component and a high-$\varepsilon_{Nd}$, incompatible-element-depleted Pacific mid-ocean ridge basalt-source-type component, since at least 30 Ma. The lack of any geochemical gradient along the chain east of Salas y Gomez implies that no systematic change over time has occurred in the proportions of these end-members.*

KEY WORDS: *Easter Seamount Chain; Nazca Ridge; Salas y Gomez Island; $^{40}Ar-^{39}Ar$ geochronology; Pb–Nd–Sr isotopic ratios*

## INTRODUCTION

The Nazca plate is unique among the smaller lithospheric plates for several reasons, one being that its western boundary is the world's fastest-spreading ocean ridge. The plate is bordered by two microplates (Easter and Juan Fernandez) and includes two relict microplates (Mendoza and Bauer) and three major seamount chains (Easter Seamount Chain, Nazca Ridge, and Carnegie Ridge) (e.g. Mayes *et al.*, 1990; Naar & Hey, 1991; Liu, 1996). It also contains four active hotspots. Of these, the Easter–Salas hotspot represents one of the few Pacific hotspots inferred by Courtillot *et al.* (2003) to have a deep, lower mantle origin, termed 'primary' hotspots. Volcanism at the Easter–Salas hotspot has produced two seamount

*Corresponding author. Telephone: +91-79-26314165. Fax: +91-79-26314900. E-mail: jsray@prl.res.in

chains on the Nazca plate: the Easter Seamount Chain (ESC) and the Nazca Ridge (NR), which together form an ~4100 km long hotspot trail (Fig. 1). The ESC is ~2900 km long, ~150 km wide, and trends roughly west–east from near the East Rift spreading axis of the Easter Microplate to the southern end of the NR. The ~1200 km long and ~300 km wide NR extends northeastward from the eastern end of the ESC to the Peru–Chile Trench (e.g. Woods & Okal, 1994).

Despite its importance as a major hotspot trail, most of the ESC–NR system has not been studied geochemically or dated, as few volcanoes in the long portion east of Salas y Gomez Island have been sampled. Thus, many questions regarding the formation and evolution of the ESC–NR system remain unresolved. In particular, questions concerning the present location of the hotspot center, the age of the system, the geochemical evolution of the hotspot source and melting conditions (depths and amounts of partial melting) that prevailed during the formation of the NR and ESC require a thorough investigation. In this work, we address these questions using new $^{40}Ar-^{39}Ar$ age determinations, major and trace element and Sr–Nd–Pb isotopic data for lavas dredged east of Salas y Gomez (from 80·3°W–105·2°W; Fig. 1) during a cruise in 2001 and in three previous cruises (see details in Samples and Analytical Methods).

## BACKGROUND

Morgan (1972) suggested that a mantle plume beneath Easter Island produces a hotspot and that the linear topographic features to the east and west of the island result from the motion of the Nazca and Pacific plates over the plume. O'Connor *et al.* (1995) provided geochronological evidence for Morgan's hypothesis. However, the results of O'Connor *et al.* (1995), based primarily on their $^{40}Ar-^{39}Ar$ age data for several samples from the ESC and one from the southwestern end of the NR, suggested that the hotspot's center is beneath or slightly to the east of Salas y Gomez, which is located 400 km east of the larger Easter Island. Alternative models to explain the ESC and/or NR include a mantle 'hot line' (Bonatti *et al.*, 1977), a leaky transform fault (e.g. Clark & Dymond, 1977), an early stage spreading center (Mammerickx, 1981) and a zone of lithospheric extension (Mammerickx & Sandwell, 1986). These hypotheses can be tested with our new geochronological data.

Lavas from Salas y Gomez and adjacent seamounts reach higher Pb and Sr and lower Nd isotopic ratios than lavas from ESC volcanoes farther west, including Easter Island, or from the rifts of the Easter Microplate (Kingsley *et al.*, 2002, 2007, and references therein). This observation has been interpreted to support the hypothesis

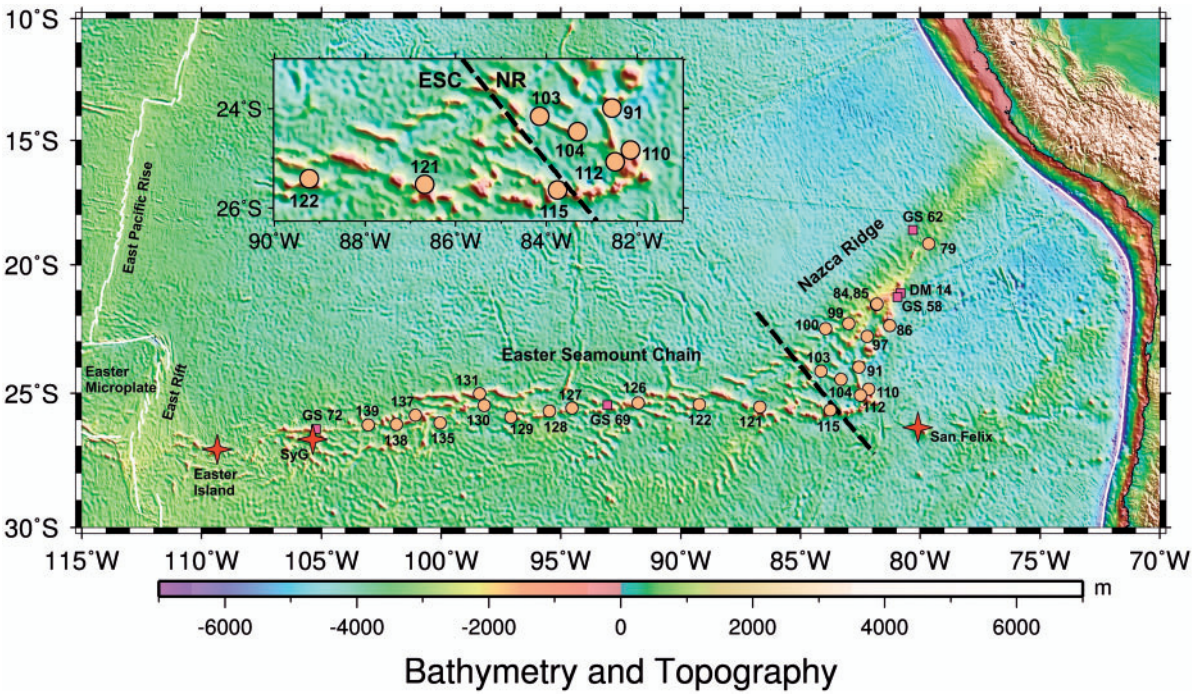


**Fig. 1.** Satellite-derived bathymetry (Smith & Sandwell, 1997) of the SE Pacific Basin, showing the Nazca Ridge, Easter Seamount Chain and other features of the Nazca plate. Locations of dredge stations from which samples of this study were obtained are marked. All samples except those labeled with DM (for R.V. *Dmitry Mendeleev* cruise 14), and GS (for GS7202) were collected during the Drift expedition. The dashed line near seamount 115 roughly marks the boundary between the NR and ESC, and the inset shows an enlarged view of the elbow region connecting the two.

that the center of the hotspot lies in the vicinity of Salas y Gomez and that the more westerly ESC volcanoes are a result of deflection of plume mantle toward the East Rift spreading axis (Hanan & Schilling, 1989; Fontignie & Schilling, 1991; Kingsley & Schilling, 1998; Kingsley *et al.*, 2002, 2007; Simons *et al.*, 2002). In contrast, Haase & Devey (1996) and Haase *et al.* (1996, 1997) argued that the hotspot's center is located at, or even somewhat west of, Easter Island. The basis of their argument was (1) the interpretation that the combined age data for the ESC, including Easter Island, revealed an apparent age progression eastward from Easter Island rather than Salas y Gomez, (2) the greater volume of Easter Island, (3) the presence of a larger number of volcanoes between the East Rift of the Easter Microplate and Easter Island than between Easter Island and Salas y Gomez, and (4) the observation that some Easter Island lavas have Nd and Sr isotopic ratios in the range of values for Salas y Gomez. Existing age data for lavas from Easter Island (0·13–2·4 Ma; O'Connor *et al.*, 1995) and Salas y Gomez (1·3–1·9 Ma; Bonatti *et al.*, 1977; Clark & Dymond, 1977) are consistent with either hypothesis. Plate and plate-motion reconstructions (Okal & Cazenave, 1985; Naar *et al.*, 1993; Kruse *et al.*, 1997; Naar & Wessel, 2000; Harada *et al.*, 2003) suggest that the hotspot center is located beneath Salas y Gomez, whereas finite-frequency seismic tomographic study by Montelli *et al.* (2006) favored a 400 km radius mantle plume centered at a position (27°S, 108°W) between Easter Island and Salas y Gomez, but closer to Easter Island. Unfortunately, the geochronological data required to settle this issue have to date been lacking.

Contrary to Morgan's (1972) plume hypothesis, in which hotspots are fixed relative to one another, recent data and modeling provide evidence of inter-hotspot motion (e.g. Koppers *et al.*, 2004; Wessel & Kroenke, 2009). Modeling by Steinberger & O'Connell (1998) and Steinberger (2002) predicts that the Easter–Salas and Hawaiian hotspots have been converging at the fastest rate of any hotspots on the planet (about 2 $cma^{-1}$). Because spreading rates between the Pacific and Nazca plates also have been the highest anywhere (~19 $cma^{-1}$ just north of the Easter Microplate; Müller *et al.*, 2008), the ages of well-dated volcanoes in these chains have the potential to resolve inter-hotspot motion. Again, however, geochronological data for the ESC–NR system have been too few. We use the new age data presented here to address the issue of hotspot fixity in a forthcoming contribution.

Previous geochemical data for ESC lavas are overwhelmingly confined to volcanoes west of Salas y Gomez and none exist for the NR (Bonatti *et al.*, 1977; Clark & Dymond, 1977; Fretzdorff *et al.*, 1996; Haase & Devey, 1996; Haase *et al.*, 1996, 1997; Kingsley & Schilling, 1998; Pan & Batiza, 1998; Cheng *et al.*, 1999; Haase, 2002; Kingsley *et al.*, 2002, 2007; Simons *et al.*, 2002). The easternmost seamount studied by Kingsley, Schilling, and coworkers is located at 102·2°W, whereas Haase and coworkers concentrated on lavas west of 109·3°W (Easter Island). In addition to data for Easter Island and Salas y Gomez Island, Cheng *et al.* (1999) reported Sr and Nd isotope ratios for nine seamount samples, and Pb isotope ratios for four of these, from a longer section of the ESC extending to 84·6°W. Several of the above studies observed systematic longitudinal variations in chemical and isotopic composition along the chain between the East Rift and Salas y Gomez. These variations have been attributed to variable mixing of two mantle sources, and/or of melts derived from these two sources, as a result of mantle flow associated with plume–ridge interaction and/or entrainment of non-plume mantle by the plume. The proposed end-members are incompatible-element-depleted mantle equivalent to that expressed along the southern East Pacific Rise (EPR) and the northern part of the East Rift, and relatively incompatible element-enriched plume mantle (e.g. Kingsley & Schilling, 1998; Cheng *et al.*, 1999; Haase, 2002; Kingsley *et al.*, 2007). The proposed plume end-member is inferred to have $^{206}Pb/^{204}Pb$ between 20·0 and 21·5, $^{87}Sr/^{86}Sr$ between 0·7030 and 0·7035 and $\varepsilon_{Nd}$ around +2.

## SAMPLES AND ANALYTICAL METHODS

The samples studied here were dredged from seamounts between 19·45°S, 80·27°W and 26·35°S, 105·23°W. Most were collected (Table 1) in 2001 during Leg 6 of the Drift expedition of the R.V. *Roger Revelle* (Naar *et al.*, 2002); data for these samples are labeled with the prefix DRFT in Tables 2–4. Six samples (GS7202 prefix) are from the University of Miami collection and were dredged by J. Dymond and J. Clark of Oregon State University. Four other samples that we used only for dating are from dredge DM14-1028 of the R.V. *Dmitry Mendeleev* cruise 14 (provided by Debra Stakes, shipboard scientist). Locations of the dredge sites are given in Tables 1 and 2. During the Drift expedition, we found that (as expected) dredging on the NR, in particular, was difficult because igneous rocks have generally been covered by pelagic sediments and ferromanganese crusts. However, we recovered igneous samples from 12 NR seamounts (dredge hauls DRFT 79–112; Fig. 1 and Table 1) and from 13 seamounts on the ESC east of Salas y Gomez (dredge hauls DRFT 115–139; Fig. 1 and Table 1). Most of these dredge hauls yielded a small amount of relatively unaltered material (glass and/or holocrystalline rock; Table 1) that we meticulously separated from ferromanganese-oxide coatings and alteration rinds containing hydrated or devitrified glass, clay minerals, carbonate, and, in some cases, abundant secondary phosphate. Most of the igneous rocks collected are either very

*Table 1: Locations, depths and recovery of DRFT06 sampling stations*

| Dredge no. | On bottom latitude (°S) | On bottom longitude (°W) | Off bottom latitude (°S) | Off bottom longitude (°W) | Distance dredged (m) | Start depth (m) | End depth (m) | Recovery* |
|---|---|---|---|---|---|---|---|---|
| 79 | 19·162 | 79·650 | 19·164 | 79·645 | 1289 | 2843 | 2567 | several glass fragments |
| 84 | 21·581 | 81·822 | 21·588 | 81·797 | 2670 | 2345 | 1400 | 3 pillow lava fragments |
| 85 | 21·562 | 81·807 | 21·567 | 81·791 | 1842 | 2290 | 1751 | 1 large pillow-glassy rind |
| 86 | 22·390 | 81·273 | 22·392 | 81·259 | 1260 | 3292 | 2755 | 1 ol./plag phyric pillow-glassy rind |
| 91 | 23·988 | 82·548 | 23·991 | 82·541 | 870 | 2823 | 2523 | 1 pillow + 2 volcanic fragments-glassy rinds |
| 97 | 22·813 | 82·211 | 22·807 | 82·199 | 1430 | 3295 | 2617 | 1 volcanic cobble |
| 100 | 22·315 | 82·976 | 22·314 | 82·966 | 1200 | 2564 | 1967 | 1 volcanic fragment |
| 101 | 22·506 | 83·948 | 22·515 | 83·955 | 2000 | 2967 | 2525 | 1 volcanic fragment-glassy rind |
| 103 | 24·156 | 84·152 | 24·174 | 84·145 | 2240 | 3479 | 2718 | 4 volcanic fragments-glassy rinds + breccia |
| 104 | 24·473 | 83·304 | 24·489 | 83·302 | 1870 | 3704 | 3190 | 1 volcanic fragment-glassy rind |
| 110 | 24·844 | 82·140 | 24·855 | 82·126 | 1872 | 2484 | 1884 | 7 volcanic fragments |
| 112 | 25·079 | 82·486 | 25·081 | 82·481 | 544 | 2748 | 2456 | 1 volcanic fragment |
| 115 | 25·647 | 83·754 | 25·651 | 83·739 | 1694 | 2442 | 1561 | 3 large basaltic fragments-glassy rinds |
| 121 | 25·531 | 86·685 | 25·544 | 86·677 | 1719 | 3088 | 2334 | several volcanic cobbles in a breccia |
| 122 | 25·420 | 89·232 | 25·421 | 89·220 | 1294 | 2690 | 2115 | plag-phyric volcanic fragments-glassy rinds + hyaloclastite + pumice |
| 126 | 25·372 | 91·761 | 25·368 | 91·749 | 1348 | 2572 | 2027 | plag-phyric volcanic fragments-glassy rinds |
| 127 | 25·560 | 94·537 | 25·569 | 94·532 | 1242 | 3221 | 2449 | 4 volcanic fragments-glassy rinds |
| 128 | 25·686 | 95·484 | 25·682 | 95·473 | 1194 | 2293 | 1597 | 3 cobbles of aphyric volcanic rock |
| 129 | 25·919 | 97·096 | 25·928 | 97·087 | 1465 | 2995 | 2252 | pillow lava fragments-glassy rinds |
| 130 | 25·457 | 98·196 | 25·462 | 98·186 | 1212 | 2969 | 2319 | 5 aphyric volcanic fragments |
| 131 | 25·024 | 98·398 | 25·024 | 98·389 | 1026 | 2043 | 1558 | pillow lava fragments + hyaloclastite |
| 135 | 26·130 | 100·046 | 26·124 | 100·036 | 1285 | 2885 | 2261 | volcanic fragments-glassy rinds |
| 137 | 25·840 | 101·079 | 25·838 | 101·071 | 884 | 2287 | 1901 | gravel with unaltered glass spherules |
| 138 | 26·175 | 101·867 | 26·186 | 101·861 | 1353 | 2773 | 2080 | volcanic fragments-glassy rinds |
| 139 | 26·195 | 103·042 | 26·192 | 103·030 | 1298 | 2100 | 1502 | volcanic fragments-glassy rinds |

*We describe only the volcanic material recovered from dredges. Almost all igneous samples were ferromanganese-encrusted. Plag, plagioclase; ol, olivine.

fine-grained aphyric or plagioclase-phyric pillow lavas, many vesicular. Besides plagioclase, other phenocrysts present in some of the samples are olivine and clinopyroxene.

We performed 40 new $^{40}Ar-^{39}Ar$ incremental heating analyses on samples from 28 seamounts along the ESC–NR, which resulted in crystallization ages between 1·4 and 30·8 Ma. Examples of the results of these detailed incremental heating experiments are displayed in age spectrum diagrams in Figs 2 and 3. Seamount locations and a summary of the $^{40}Ar-^{39}Ar$ ages are listed in Tables 1 and 2. Full measurement data can be accessed and downloaded from the EarthRef.org Digital Archive (ERDA) by simply searching for sample numbers or names of seamount chains. The data files are provided in Microsoft Excel format.

For our $^{40}Ar-^{39}Ar$ work, we analyzed whole-rocks and plagioclase and groundmass separates prepared from the dredged rocks. In several cases we were able to analyze plagioclase and groundmass or whole-rock from the same sample, from which we could assess the age reproducibility and accuracy. Visible alteration was removed from the samples with a rock saw. We then crushed the samples using a porcelain jaw crusher, stainless steel ring mill and in some cases a porcelain hand mortar until ~25% of the grains were sieved into the 210–300 μm fraction. This size fraction was rinsed several times using ultra-pure deionized water and set in a 40°C oven to dry overnight. Some groundmass samples were further processed using a Frantz magnetic separator to separate plagioclase. Finally, all samples were cleaned by leaching in 1M HCl (60 min),

*Table 2:* $^{40}Ar-^{39}Ar$ *incremental heating ages of volcanic material from the Nazca Ridge and Easter Seamount Chain and* Δ *crust ages for the seamounts*

| Sample | Material | Latitude (°S) | Longitude (°W) | Plateau age (Ma) | ±2σ | Isochron age (Ma) | ±2σ | Total fusion age (Ma) | ±2σ | Δ crust age (Ma) |
|---|---|---|---|---|---|---|---|---|---|---|
| DRFT-84-1 | groundmass | 21·58 | 81·82 | 4·48 | 0·04 | 4·43 | 0·16 | 4·06 | 0·05 | 31·43 |
| DRFT-85-1 | groundmass | 21·56 | 81·81 | 5·00 | 0·08 | 4·94 | 0·13 | 5·00 | 0·10 | 30·63 |
| DRFT-86-1 | plagioclase | 22·39 | 81·27 | 27·43 | 1·80 | | | 30·36 | 1·23 | 12·46 |
| DRFT-91-2 | groundmass | 23·99 | 82·55 | 23·85 | 0·13 | 23·85 | 0·15 | 22·28 | 0·11 | 12·02 |
| DRFT-97-1 | plagioclase | 22·81 | 82·21 | 24·58 | 0·50 | 24·79 | 0·95 | 24·40 | 0·53 | 13·18 |
| DRFT-100-2 | whole rock | 22·31 | 82·98 | | | | | *24·32* | *0·69* | 12·49 |
| DRFT-101-1 | groundmass | 22·51 | 83·95 | | | | | *11·81* | *0·25* | |
| DRFT-101-1 | plagioclase | 22·51 | 83·95 | 27·47 | 7·45 | 33·63 | 69·75 | 103·04 | 12·81 | 5·94 |
| DRFT-103-2 | whole rock | 24·17 | 84·17 | 24·92 | 0·20 | 24·84 | 0·27 | 20·80 | 0·15 | 7·90 |
| DRFT-104-4 | whole rock | 24·47 | 83·30 | 24·13 | 0·56 | 23·89 | 0·51 | 23·09 | 0·90 | 9·77 |
| DRFT-110-3 | groundmass | 24·83 | 82·11 | | | | | *23·40* | *0·10* | |
| DRFT-110-7 | plagioclase | 24·83 | 82·11 | 25·49 | 0·59 | 23·97 | 0·15 | 27·20 | 0·43 | 10·25 |
| DRFT-112-1 | groundmass | 25·08 | 82·49 | 23·49 | 0·29 | 23·60 | 0·42 | 24·99 | 0·46 | 11·23 |
| DRFT-115-1 | whole rock | 25·65 | 83·75 | | | | | *13·59* | *0·07* | |
| DRFT-115-2 | groundmass | 25·65 | 83·75 | | | 16·27 | 0·19 | 16·32 | 0·13 | 15·90 |
| DRFT-121-1 | groundmass | 25·53 | 86·69 | 19·01 | 0·23 | 19·05 | 0·32 | 18·82 | 0·15 | |
| DRFT-121-1 | plagioclase | 25·53 | 86·69 | 19·19 | 0·09 | 19·20 | 0·11 | 19·20 | 0·09 | 9·11 |
| DRFT-122-1 | plagioclase | 25·42 | 89·23 | 17·62 | 0·70 | 17·18 | 0·80 | 18·20 | 0·58 | 7·10 |
| DRFT-126-1 | plagioclase | 25·37 | 91·76 | | | 15·82 | 8·06 | 30·39 | 1·37 | 4·01 |
| DRFT-126-5 | whole rock | 25·37 | 91·76 | | | | | *14·85* | *1·89* | |
| DRFT-127-2 | whole rock | 25·56 | 94·54 | 12·16 | 0·09 | 12·17 | 0·22 | 12·31 | 0·19 | 5·79 |
| DRFT-128-2 | whole rock | 25·69 | 95·48 | 10·97 | 0·11 | 10·95 | 0·16 | 10·14 | 0·21 | 6·44 |
| DRFT-129-1 | plagioclase | 25·92 | 97·10 | 9·52 | 0·48 | 9·47 | 0·68 | 12·32 | 0·44 | 6·79 |
| DRFT-130-1 | whole rock | 25·46 | 98·20 | 10·67 | 1·25 | 5·85 | 3·47 | 11·28 | 1·06 | 4·79 |
| DRFT-130-2 | whole rock | 25·46 | 98·20 | | | 11·52 | 1·10 | 15·78 | 1·43 | |
| DRFT-131-1 | groundmass | 25·02 | 98·40 | 10·59 | 0·21 | 10·37 | 0·23 | 9·72 | 0·17 | 4·77 |
| DRFT-135-1 | whole rock | 26·13 | 100·05 | 6·53 | 0·09 | 6·50 | 0·07 | 6·69 | 0·44 | 7·52 |
| DRFT-138-3 | whole rock | 26·17 | 101·87 | 4·41 | 0·27 | 4·37 | 0·45 | 4·37 | 0·40 | 8·31 |
| DRFT-139-4 | plagioclase | 26·19 | 103·04 | 2·78 | 0·32 | 2·70 | 0·37 | 3·10 | 0·28 | 9·05 |
| DM14-1028-3 | plagioclase | 21·12 | 80·83 | 20·29 | 0·85 | 19·92 | 1·60 | 26·39 | 1·10 | 17·12 |
| DM14-1028-11 | whole rock | 21·12 | 80·83 | | | | | *25·28* | *0·38* | |
| DM14-1028-37 | plagioclase | 21·12 | 80·83 | 28·45 | 4·12 | 26·11 | 6·12 | 41·26 | 4·31 | |
| GS7202 DR62-1 | whole rock | 18·62 | 80·30 | 29·86 | 0·29 | 29·77 | 0·40 | 26·12 | 0·24 | |
| GS7202 DR62-2 | whole rock | 18·62 | 80·30 | 30·74 | 0·80 | 30·25 | 1·65 | 26·05 | 0·22 | 8·99 |
| GS7202 DR62A | whole rock | 18·62 | 80·30 | 26·66 | 0·20 | 26·58 | 0·49 | 26·66 | 0·22 | |
| GS7202 DR58 | whole rock | 21·28 | 80·95 | 21·59 | 2·14 | 23·34 | 4·47 | 20·48 | 0·47 | 18·13 |
| GS7202 DR72-2 | whole rock | 26·35 | 105·23 | 1·35 | 0·02 | 1·33 | 0·03 | 1·28 | 0·02 | 8·65 |
| GS7202 DR69-2 | groundmass | 25·44 | 93·05 | 12·51 | 1·3 | 12·38 | 1·44 | 15·33 | 2·35 | |

DRFT samples were collected during the Drift 06 expedition in 2001. DM samples are from cruise 14 of the R.V. *Dmitry Mendeleev* and GS7202 samples are from the dredged rock collection at the University of Miami. For DRFT 79-1, an age of 30·0 Ma for the seamount is interpolated using the age–distance relationship in Fig. 3. Italicized total fusion ages are best estimates for whole-rock and groundmass samples that exhibit $^{39}Ar$ and $^{37}Ar$ recoil. Δ crust age = age of the underlying seafloor – age of the seamount. The age of the crust below seamounts is estimated following Müller *et al.* (2008).

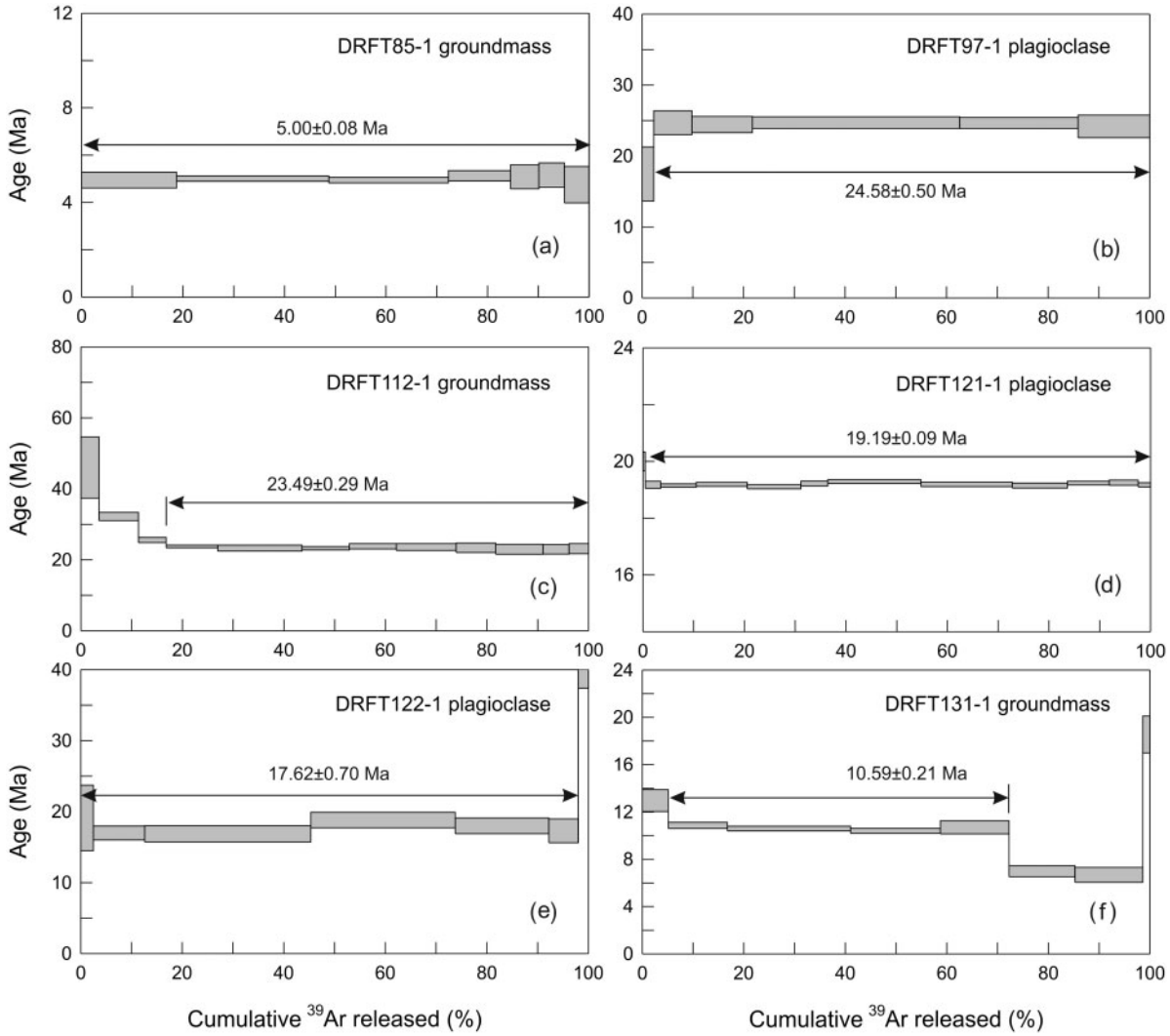


**Fig. 2.** Step-heating $^{40}Ar-^{39}Ar$ apparent age spectra for plagioclase and groundmass samples of dredged rocks from the ESC and NR (a–f). Plateau ages (which are the weighted means of contiguous, concordant step ages comprising >50% of the total gas released) are indicated.

6M HCl (60 min), 1M $HNO_3$ (60 min) and ultra-pure deionized water (60 min) in an ultrasonic bath heated to ~50°C. Before irradiation we hand-picked ~100 mg of groundmass for each sample using a binocular microscope to remove any grains containing (remaining) alteration or parts of mafic phenocrysts and microcrysts, which can be sources of excess mantle-derived $^{40}Ar$. Plagioclase samples were prepared in the same way except that the acid leaching included an extra step with ~2·5M HF (15 min) to gently etch away the (altered) rims of the crystals. We separated ~50 mg of plagioclase from each sample.

The prepared samples were irradiated for 6 h in the TRIGA nuclear reactor at Oregon State University, along with the FCT-3 biotite (28·03 ± 0·18 Ma, 1σ) flux monitor (Renne *et al.*, 1998). J-values for each sample were calculated by parabolic extrapolation of the measured flux gradient against irradiation height and typically give 0·3–0·5% uncertainties (1σ). We performed $^{40}Ar-^{39}Ar$ incremental heating age determinations using either a double-vacuum resistance furnace fitted with a thermocouple or a continuous 10 W $CO_2$ laser probe, combined with a MAP-215/50 mass spectrometer at Oregon State University. Irradiated samples were loaded into a glass manifold that fed into the Ta-crucible of the furnace, or into a Cu-planchette in an ultrahigh-vacuum sample chamber, and incrementally heated by scanning a defocused $CO_2$ laser beam in preset patterns across the sample to evenly release the argon gas. After heating, reactive gases were removed using an SAES Zr-Al ST101 GP50 getter operated at 400°C for ~15 min and two SAES Fe–V–Zr ST172 getters operated at 200°C and room temperature, respectively. We measured system

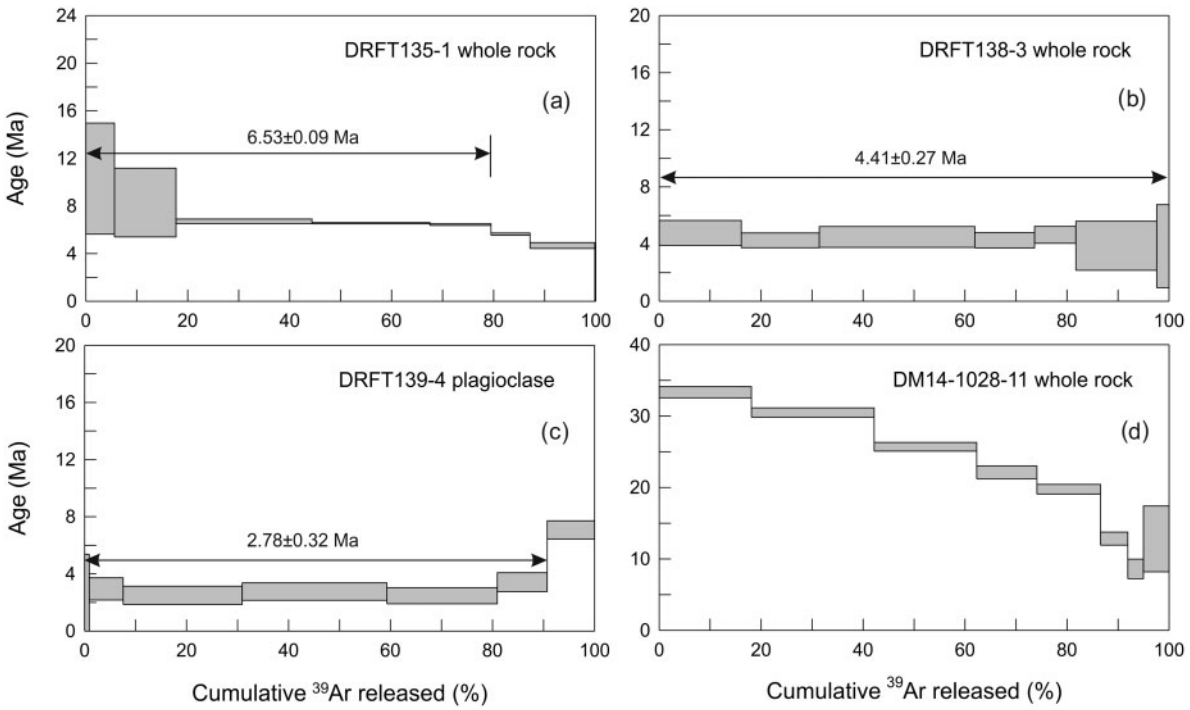


**Fig. 3.** Step-heating $^{40}$Ar–$^{39}$Ar apparent age spectra for plagioclase and whole-rock samples of dredged rocks from the ESC and NR (a–d). Plateau ages are indicated. Panel (d) shows an example of an experiment affected by recoil ($^{37}$Ar, $^{39}$Ar).

blanks before analyzing each sample. Data peak intensities were reduced using linear or exponential curve fits with respect to the inlet time of the gas sample into the mass spectrometer. All ages were calculated using the Steiger & Jäger (1977) decay constants. For a detailed description of the analytical facility and the constants used in the age calculations we refer to table 2 of Koppers *et al.* (2003).

Incremental heating plateau ages and isochron ages were calculated as weighted means with $1/\sigma^2$ as a weighting factor (Taylor, 1997) and as YORK2 least-square fits with correlated errors (York, 1969) using the ArArCALC v2.5 software from Koppers (2002) that is available from the http://earthref.org/tools/ararcalc.htm web site. Plateau ages and isochrons with MSWD higher than unity were taken to indicate an increased scatter owing to geological uncertainties beyond the precision of the increment ages themselves. In these cases, the reported analytical errors are multiplied by the $\sqrt{}$MSWD (York, 1969; Kullerud, 1991). All errors on the $^{40}$Ar–$^{39}$Ar ages are reported at the 95% confidence level ($2\sigma$), unless otherwise indicated. Contiguous, concordant step ages, especially over the middle- to high-temperature portion of the gas release spectrum, form a plateau age. The isochron age is calculated from the slope of collinear step compositions plotted in a $^{40}$Ar/$^{36}$Ar vs $^{39}$Ar/$^{36}$Ar correlation diagram. A reliable sample crystallization age is concluded if the plateau and isochron ages are concordant within analytical uncertainty, and indicate no significant presence of mantle-derived ('excess') Ar. In such cases we generally prefer the plateau age, being more precise than the isochron age, which is often affected by small dispersion in highly radiogenic step compositions. We calculated total fusion ages by summing all step gas compositions, as if the experiment consisted of a single step. A total fusion age provides a useful reference in case of Ar-recoil.

Submarine samples typically are subjected to some (high) degree of alteration. However, Ar loss related to such low-temperature, partial replacement of igneous phases with (typically) clays, zeolites, and calcite can be mitigated with $^{40}$Ar–$^{39}$Ar incremental heating procedures. We can assess our ability to derive reliable crystallization ages from such rocks in each experiment, but also through comparison of multiple age determinations on individual rocks or rocks from the same or closely grouped dredge hauls (Table 2). For example, DRFT 121-1 provided ages of 19·01 ± 0·23 Ma (groundmass) and 19·19 ± 0·09 Ma (plagioclase), and rocks from dredges GS7202 DR62-1 and 2 were dated at 29·86 ± 0·29 Ma and 30·74 ± 0·80 Ma, respectively.

Major and trace element contents (Table 3) and isotopic ratios (Table 4) were measured at the University of Hawaii on phenocryst-free chips of handpicked glass or on alumina-ground powders of handpicked chips of the least-altered, relatively phenocryst-free holocrystalline

*Table 3: Chemical compositions of lavas from the Nazca Ridge and Easter Seamount Chain*

| Sample: | 79-1 g | 84-1wr | 85-1 g | 86-1 g | 91-1 g | 101-2 g | 103-3 g | 104-1 g | 112-1wr |
|---|---|---|---|---|---|---|---|---|---|
| $SiO_2$ | 49·43 | 44·16 | 42·29 | 49·16 | 48·75 | 48·67 | 48·11 | 47·31 | 40·90 |
| $TiO_2$ | 2·03 | 3·20 | 3·92 | 2·74 | 2·92 | 1·15 | 2·75 | 2·56 | 3·21 |
| $Al_2O_3$ | 16·85 | 13·42 | 14·15 | 14·15 | 16·67 | 16·64 | 17·07 | 16·52 | 15·93 |
| $FeO^T$ | 8·95 | 11·28 | 11·15 | 12·11 | 10·23 | 10·45 | 10·35 | 11·5 | 10·91 |
| MnO | 0·15 | 0·17 | 0·22 | 0·20 | 0·15 | 0·18 | 0·16 | 0·20 | 0·15 |
| MgO | 7·14 | 9·31 | 5·03 | 6·33 | 5·95 | 8·85 | 6·02 | 6·57 | 2·48 |
| CaO | 11·18 | 11·34 | 11·18 | 11·33 | 9·81 | 12·7 | 8·97 | 10·19 | 15·36 |
| $Na_2O$ | 3·09 | 3·42 | 5·76 | 2·67 | 3·48 | 2·34 | 3·88 | 3·36 | 3·05 |
| $K_2O$ | 0·85 | 2·54 | 3·38 | 0·50 | 1·10 | 0·04 | 1·05 | 0·64 | 1·51 |
| $P_2O_5$ | 0·31 | 1·11 | 1·96 | 0·31 | 0·50 | 0·08 | 0·52 | 0·32 | 6·04 |
| Total | 99·98 | 99·94 | 99·04 | 99·50 | 99·56 | 101·10 | 98·88 | 99·17 | 99·54 |
| LOI | | 2·07 | | | | | | | 5·57 |
| Cs | 0·31 | 1·26 | 1·78 | 0·21 | 0·46 | 0·01 | 0·44 | 0·27 | 0·29 |
| Rb | 22·5 | 52·7 | 63·9 | 11·6 | 26·7 | 0·2 | 25·8 | 15·7 | 19·7 |
| Ba | 202 | 532 | 610 | 88 | 242 | 4 | 217 | 136 | 346 |
| Th | 2·5 | 6·2 | 10·3 | 1·1 | 2·6 | 0·0 | 2·8 | 1·5 | 4·2 |
| U | 0·66 | 1·96 | 3·33 | 0·37 | 0·81 | 0·01 | 0·90 | 0·49 | 2·84 |
| Nb | 38 | 105 | 177 | 22 | 45 | 1 | 43 | 27 | 59 |
| Ta | 2·01 | 5·41 | 8·98 | 1·29 | 2·52 | 0·08 | 2·48 | 1·48 | 3·72 |
| La | 25 | 71 | 114 | 15 | 29 | 1 | 28 | 18 | 46 |
| Ce | 48 | 135 | 212 | 36 | 61 | 5 | 59 | 39 | 93 |
| Pr | 5·6 | 16·1 | 25·1 | 5·0 | 7·6 | 0·9 | 7·5 | 5·1 | 12·7 |
| Pb | 1·3 | 6·2 | 5·7 | 0·8 | 1·4 | 0·2 | 1·4 | 0·9 | 7·4 |
| Sr | 327 | 976 | 1367 | 274 | 431 | 84 | 384 | 338 | 810 |
| Nd | 22 | 62 | 97 | 23 | 32 | 6 | 32 | 22 | 51 |
| Hf | 3·4 | 7·7 | 11·9 | 4·4 | 5·5 | 1·5 | 5·9 | 4·0 | 8·0 |
| Zr | 142 | 378 | 589 | 184 | 243 | 47 | 259 | 180 | 364 |
| Sm | 4·9 | 11·7 | 17·6 | 5·9 | 7·0 | 2·3 | 7·3 | 5·4 | 10·2 |
| Eu | 1·5 | 3·4 | 4·9 | 1·9 | 2·3 | 0·9 | 2·3 | 1·8 | 3·3 |
| Gd | 5·2 | 10·9 | 16·2 | 6·4 | 7·3 | 3·2 | 7·9 | 6·1 | 9·9 |
| Tb | 0·81 | 1·39 | 2·06 | 1·02 | 1·09 | 0·62 | 1·19 | 0·96 | 1·44 |
| Dy | 4·7 | 6·8 | 10·1 | 5·7 | 6·0 | 4·0 | 6·7 | 5·6 | 7·7 |
| Y | 28·1 | 33·8 | 48·9 | 33·0 | 32·6 | 25·8 | 38·4 | 34·6 | 40·7 |
| Ho | 0·97 | 1·15 | 1·67 | 1·18 | 1·14 | 0·94 | 1·34 | 1·18 | 1·52 |
| Er | 2·6 | 2·8 | 4·0 | 2·9 | 2·8 | 2·6 | 3·4 | 3·0 | 3·8 |
| Tm | 0·4 | 0·4 | 0·5 | 0·4 | 0·4 | 0·4 | 0·5 | 0·4 | 0·5 |
| Yb | 2·5 | 2·2 | 3·2 | 2·6 | 2·5 | 2·6 | 3·1 | 2·8 | 3·4 |
| Lu | 0·37 | 0·32 | 0·46 | 0·39 | 0·37 | 0·4 | 0·46 | 0·43 | 0·53 |
| Sc | 39·3 | 26·2 | 13·3 | 53·5 | 27·1 | 41·4 | 21·2 | 32·5 | |
| Cr | 219 | 263 | 475 | 200 | 128 | 306 | 107 | 165 | |
| Co | 42 | 48 | 48 | 48 | 38 | 50 | 37 | 46 | |
| Ni | 121 | 180 | 288 | 65 | 90 | 152 | 93 | 126 | |
| Zn | 81 | 129 | 144 | 115 | 102 | 70 | 101 | 106 | |

(continued)

*Table 3: Continued*

| Sample: | 115-1 g | 121-1wr | 122-1 g | 126-1 g | 127-1wr | 127-4 g | 129-1 g | 130-1 g | 130-4 g |
|---|---|---|---|---|---|---|---|---|---|
| $SiO_2$ | 50·04 | 64·50 | 48·98 | 49·22 | 51·60 | 53·86 | 48·03 | 49·99 | 50·00 |
| $TiO_2$ | 2·94 | 0·70 | 3·48 | 2·56 | 2·23 | 2·25 | 3·32 | 1·38 | 1·69 |
| $Al_2O_3$ | 18·07 | 14·55 | 14·37 | 14·98 | 17·62 | 15·63 | 15·53 | 16·19 | 14·90 |
| $FeO^T$ | 8·17 | 8·28 | 12·8 | 11·71 | 9·77 | 8·97 | 12·13 | 9·56 | 10·48 |
| MnO | 0·15 | 0·30 | 0·22 | 0·20 | 0·14 | 0·18 | 0·19 | 0·17 | 0·21 |
| MgO | 3·46 | 0·51 | 4·97 | 6·46 | 4·99 | 4·36 | 5·78 | 8·45 | 7·42 |
| CaO | 6·87 | 1·41 | 9·94 | 11·07 | 9·66 | 8·18 | 10·04 | 12·14 | 12·52 |
| $Na_2O$ | 4·94 | 4·93 | 3·19 | 2·92 | 2·97 | 3·67 | 3·28 | 2·56 | 2·97 |
| $K_2O$ | 3·58 | 4·91 | 0·92 | 0·51 | 0·76 | 1·63 | 0·96 | 0·09 | 0·13 |
| $P_2O_5$ | 1·07 | 0·07 | 0·51 | 0·30 | 0·32 | 0·30 | 0·46 | 0·11 | 0·16 |
| Total | 99·29 | 100·16 | 99·38 | 99·93 | 100·06 | 99·04 | 99·72 | 100·64 | 100·47 |
| LOI | | 6·07 | | | 3·26 | | | | |
| | 115-1wr | | | | | | | | |
| Cs | 0·23 | 1·00 | 2·17 | 0·14 | 0·70 | 0·53 | 0·16 | 0·01 | 0·02 |
| Rb | 34·8 | 61·0 | 16·5 | 9·9 | 11·3 | 35·3 | 8·1 | 0·5 | 1·0 |
| Ba | 543 | 137 | 116 | 95 | 206 | 262 | 133 | 8 | 12 |
| Th | 7·5 | 6·2 | 1·7 | 1·1 | 4·0 | 4·1 | 2·1 | 0·2 | 0·2 |
| U | 1·19 | 1·57 | 0·64 | 0·37 | 0·62 | 1·34 | 0·53 | 0·06 | 0·08 |
| Nb | 87 | 97 | 29 | 21 | 53 | 56 | 34 | 4 | 5 |
| Ta | 5·23 | 5·25 | 1·79 | 1·24 | 3·07 | 3·09 | 1·98 | 0·24 | 0·31 |
| La | 73 | 53 | 20 | 14 | 37 | 38 | 22 | 3 | 5 |
| Ce | 135 | 122 | 45 | 32 | 75 | 79 | 47 | 10 | 15 |
| Pr | 15·0 | 14·4 | 6·2 | 4·5 | 9·7 | 10·0 | 6·2 | 1·5 | 2·2 |
| Pb | 5·6 | 3·8 | 1·5 | 0·8 | 2·1 | 2·1 | 1·3 | 0·5 | 0·5 |
| Sr | 864 | 17 | 352 | 265 | 274 | 249 | 425 | 149 | 172 |
| Nd | 56 | 57 | 27 | 21 | 40 | 41 | 27 | 8 | 12 |
| Hf | 8·7 | 14·0 | 5·1 | 4·1 | 9·5 | 9·6 | 4·7 | 2·0 | 2·7 |
| Zr | 374 | 625 | 208 | 169 | 373 | 428 | 197 | 75 | 115 |
| Sm | 9·8 | 12·3 | 6·6 | 5·4 | 8·9 | 9·1 | 6·1 | 2·7 | 3·8 |
| Eu | 2·8 | 3·4 | 2·2 | 1·8 | 2·5 | 2·4 | 2·0 | 1·0 | 1·3 |
| Gd | 9·2 | 12·3 | 7·3 | 6·1 | 9·7 | 9·9 | 6·5 | 3·5 | 4·6 |
| Tb | 1·18 | 1·91 | 1·14 | 0·99 | 1·56 | 1·57 | 1·00 | 0·63 | 0·84 |
| Dy | 6·1 | 10·6 | 6·4 | 5·7 | 8·8 | 8·9 | 5·4 | 3·9 | 5·2 |
| Y | 30·6 | 58·9 | 36·9 | 33·3 | 55·5 | 54·2 | 28·7 | 24·9 | 34·7 |
| Ho | 1·03 | 2·12 | 1·31 | 1·17 | 1·85 | 1·85 | 1·07 | 0·90 | 1·15 |
| Er | 2·6 | 5·6 | 3·4 | 3·0 | 4·9 | 4·8 | 2·6 | 2·3 | 3·1 |
| Tm | 0·4 | 0·9 | 0·5 | 0·4 | 0·7 | 0·7 | 0·4 | 0·4 | 0·5 |
| Yb | 2·2 | 5·6 | 3·1 | 2·8 | 4·7 | 4·7 | 2·3 | 2·3 | 3·0 |
| Lu | 0·32 | 0·90 | 0·47 | 0·42 | 0·71 | 0·69 | 0·35 | 0·35 | 0·45 |
| Sc | 10·1 | | 34·3 | 38·9 | 26·3 | 22·3 | 22·7 | 34·8 | 49·7 |
| Cr | | | 87 | 222 | 141 | 92 | 94 | 339 | 286 |
| Co | 32 | | 33 | 47 | 24 | 27 | 30 | 46 | 51 |
| Ni | 72 | | 31 | 70 | 46 | 50 | 40 | 131 | 62 |
| Zn | 125 | 147 | 139 | 107 | 131 | 106 | 102 | 69 | 85 |

(continued)

*Table 3: Continued*

| Sample: | 130-5 g | 131-1wr | 135-4wr | 135-6 g | 137-2 g | 138-1 g | 138-3wr | 139-1 g |
|---|---|---|---|---|---|---|---|---|
| $SiO_2$ | 49·16 | 46·78 | 50·40 | 50·77 | 47·44 | 47·05 | 47·09 | 48·19 |
| $TiO_2$ | 2·92 | 2·79 | 3·08 | 3·04 | 3·97 | 2·08 | 1·49 | 4·35 |
| $Al_2O_3$ | 15·33 | 17·69 | 15·53 | 14·99 | 15·55 | 16·87 | 16·12 | 15·45 |
| $FeO^T$ | 11·68 | 10·54 | 11·31 | 11·78 | 12·50 | 10·96 | 10·71 | 12·32 |
| MnO | 0·19 | 0·15 | 0·14 | 0·25 | 0·18 | 0·19 | 0·16 | 0·18 |
| MgO | 5·85 | 6·90 | 4·01 | 3·49 | 5·33 | 7·88 | 10·52 | 4·91 |
| CaO | 10·21 | 11·42 | 8·33 | 7·75 | 9·24 | 11·64 | 11·79 | 9·12 |
| $Na_2O$ | 3·15 | 2·39 | 3·62 | 4·25 | 3·53 | 2·70 | 1·94 | 3·57 |
| $K_2O$ | 0·86 | 0·69 | 1·52 | 1·90 | 1·06 | 0·38 | 0·29 | 1·34 |
| $P_2O_5$ | 0·39 | 0·68 | 1·64 | 1·33 | 0·55 | 0·21 | 0·10 | 0·64 |
| Total | 99·74 | 100·03 | 99·58 | 99·55 | 99·35 | 99·96 | 100·20 | 100·07 |
| LOI | | 2·29 | 3·28 | | | | 0·04 | |
| Cs | 0·02 | 0·11 | 2·51 | | 0·37 | 0·13 | 0·27 | 0·45 |
| Rb | 0·8 | 8·4 | 25·6 | | 23·7 | 8·3 | 5·6 | 24·5 |
| Ba | 11 | 212 | 348 | | 207 | 81 | 39 | 256 |
| Th | 0·2 | 3·8 | 4·6 | | 2·7 | 1·0 | 0·5 | 3·3 |
| U | 0·08 | 1·07 | 1·12 | | 0·86 | 0·29 | 0·18 | 1·09 |
| Nb | 5 | 47 | 80 | | 46 | 18 | 9 | 55 |
| Ta | 0·28 | 2·87 | 4·58 | | 2·83 | 1·05 | 0·63 | 3·22 |
| La | 5 | 33 | 58 | | 29 | 11 | 6 | 35 |
| Ce | 14 | 65 | 120 | | 63 | 25 | 14 | 73 |
| Pr | 2·0 | 8·4 | 15·6 | | 8·5 | 3·5 | 2·0 | 9·4 |
| Pb | 0·5 | 8·7 | 3·6 | | 1·4 | 0·6 | 0·5 | 2·3 |
| Sr | 168 | 524 | 400 | | 341 | 239 | 177 | 470 |
| Nd | 11 | 33 | 67 | | 37 | 15 | 10 | 39 |
| Hf | 2·6 | 5·0 | 9·7 | | 6·9 | 3·0 | 2·2 | 7·3 |
| Zr | 109 | 216 | 427 | | 283 | 121 | 82 | 314 |
| Sm | 3·5 | 7·5 | 15·0 | | 8·5 | 4·0 | 3·0 | 8·9 |
| Eu | 1·3 | 2·4 | 4·4 | | 2·7 | 1·4 | 1·1 | 2·8 |
| Gd | 4·4 | 7·2 | 15·9 | | 9·0 | 4·8 | 3·8 | 9·4 |
| Tb | 0·80 | 1·06 | 2·37 | | 1·36 | 0·80 | 0·67 | 1·37 |
| Dy | 5·0 | 6·0 | 12·5 | | 7·4 | 4·7 | 4·1 | 7·5 |
| Y | 34·3 | 32·9 | 69·4 | | 39·6 | 27·7 | 24·5 | 40·6 |
| Ho | 1·11 | 1·21 | 2·45 | | 1·45 | 1·01 | 0·93 | 1·41 |
| Er | 3·0 | 3·1 | 6·0 | | 3·6 | 2·6 | 2·4 | 3·5 |
| Tm | 0·5 | 0·5 | 0·9 | | 0·5 | 0·4 | 0·4 | 0·5 |
| Yb | 2·9 | 2·9 | 5·2 | | 3·2 | 2·6 | 2·4 | 3·1 |
| Lu | 0·43 | 0·48 | 0·77 | | 0·48 | 0·40 | 0·38 | 0·46 |
| Sc | 49·1 | | 28 | | 25·4 | 35 | 37·7 | 30·5 |
| Cr | 319 | | | | 42 | 181 | 374 | 37 |
| Co | 52 | | 20 | | 35 | 49 | 64 | 29 |
| Ni | 71 | | | | 45 | 126 | 305 | 30 |
| Zn | 83 | | 141 | | 118 | 81 | 74 | 113 |

(continued)

*Table 3: Continued*

| Sample: | D-58wr | D-62wr | D-72wr | JB-1 A(m) | JB-1 A(r) |
|---|---|---|---|---|---|
| $SiO_2$ | 46·88 | 49·55 | 53·33 | 53·58 | 53·70 |
| $TiO_2$ | 1·92 | 2·24 | 2·09 | 1·32 | 1·33 |
| $Al_2O_3$ | 16·48 | 18·25 | 18·32 | 14·87 | 14·81 |
| $FeO^T$ | 12·80 | 9·18 | 7·76 | 8·35 | 8·23 |
| MnO | 0·15 | 0·14 | 0·14 | 0·14 | 0·15 |
| MgO | 5·17 | 7·17 | 3·59 | 7·97 | 8·07 |
| CaO | 13·02 | 9·14 | 5·75 | 9·57 | 9·54 |
| $Na_2O$ | 2·22 | 3·04 | 4·92 | 2·63 | 2·68 |
| $K_2O$ | 0·29 | 0·95 | 2·91 | 1·42 | 1·41 |
| $P_2O_5$ | 1·19 | 0·38 | 0·99 | 0·26 | 0·26 |
| Total | 100·11 | 100·03 | 99·79 | 100·13 | 100·19 |
| LOI | 2·47 | 1·85 | 0·86 | | |
| | | | | BHVO-1(m) | BHVO-1(r) |
| Cs | 0·13 | 0·62 | 1·12 | 0·13 | 0·10 |
| Rb | 3·2 | 18·6 | 68·5 | 9·8 | 9·5 |
| Ba | 43 | 256 | 708 | 133 | 133 |
| Th | 1·0 | 3·0 | 9·6 | 1·1 | 1·3 |
| U | 1·47 | 0·73 | 2·51 | 0·42 | 0·42 |
| Nb | 11 | 38 | 118 | 19 | 20 |
| Ta | 0·76 | 2·37 | 7·43 | 1·15 | 1·20 |
| La | 10 | 23 | 71 | 16 | 16 |
| Ce | 23 | 46 | 134 | 38 | 38 |
| Pr | 3·5 | 5·8 | 15·8 | 5·4 | 5·5 |
| Pb | 0·6 | 1·6 | 4·4 | 2·1 | 2·1 |
| Sr | 255 | 464 | 801 | 369 | 390 |
| Nd | 16 | 22 | 56 | 25 | 25 |
| Hf | 3·4 | 3·9 | 8·9 | 4·4 | 4·3 |
| Zr | 126 | 173 | 411 | 169 | 180 |
| Sm | 4·6 | 5·0 | 10·0 | 6·1 | 6·1 |
| Eu | 1·6 | 1·8 | 3·2 | 2·0 | 2·1 |
| Gd | 5·7 | 5·6 | 8·8 | 6·4 | 6·2 |
| Tb | 0·98 | 0·87 | 1·22 | 0·96 | 0·95 |
| Dy | 5·9 | 5·0 | 6·5 | 5·2 | 5·3 |
| Y | 32·5 | 25·6 | 31·1 | 27·3 | 28·0 |
| Ho | 1·27 | 1·07 | 1·25 | 0·99 | 1·00 |
| Er | 3·4 | 2·8 | 3·2 | 2·4 | 2·6 |
| Tm | 0·5 | 0·4 | 0·5 | 0·3 | |
| Yb | 3·3 | 2·8 | 3·0 | 2·0 | 2·0 |
| Lu | 0·53 | 0·45 | 0·47 | 0·29 | 0·28 |
| Sc | | | | 32·5 | 31·8 |
| Cr | | | | 292 | 289 |
| Co | | | | 45 | 45 |
| Ni | | | | 123 | 120 |
| Zn | | | | 107 | 105 |

g, glass; wr, whole-rock. Major element oxides are in wt %; trace elements are in ppm. Total iron is reported as ferrous oxide ($FeO^T$). LOI is per cent weight loss on ignition to 900°C for 24 h. For the major oxides, relative precision is 1%, except for $SiO_2$, for which it is 0·5%. For trace elements, precision is <5% at levels in the rock above about 0·3 ppm; for Ta concentrations less than about 0·3 ppm, it is about 25%. A comparison of measured (m, mean of 15 analyses) and recommended (r) values for standards JB-1A (Govindraju, 1994) for major oxides and BHVO-1 (Eggins *et al.*, 1997) for trace elements is given as an indication of accuracy.

*Table 4: Radiogenic isotope data for lavas from the Nazca Ridge and Easter Seamount Chain*

| Sample | $^{87}Sr/^{86}Sr_m$ | $^{143}Nd/^{144}Nd_m$ | $\varepsilon_{Ndm}$ | $^{206}Pb/^{204}Pb_m$ | $^{207}Pb/^{204}Pb_m$ | $^{208}Pb/^{204}Pb_m$ | Pb (ppm) | $^{238}U/^{204}Pb_m$ | $^{232}Th/^{204}Pb_m$ | $^{87}Sr/^{86}Sr_t$ | $\varepsilon_{Nd}(t)$ | $^{206}Pb/^{204}Pb_t$ | $^{207}Pb/^{204}Pb_t$ | $^{208}Pb/^{204}Pb_t$ |
|---|---|---|---|---|---|---|---|---|---|---|---|---|---|---|
| 79-1g | 0·70320 | 0·512917 | 5·4 | 19·729 | 15·640 | 39·529 | 1·44 | 30·10 | 117·8 | 0·70311 | 5·6 | 19·589 | 15·633 | 39·354 |
| 84-1wr | 0·70382 | 0·512809 | 3·3 | 19·466 | 15·617 | 39·277 | 4·47 | 28·56 | 93·3 | 0·70381 | 3·3 | 19·446 | 15·616 | 39·256 |
| 85-1g | 0·70389 | 0·512784 | 2·8 | 19·764 | 15·643 | 39·560 | 6·46 | 33·84 | 108·2 | 0·70388 | 2·9 | 19·738 | 15·642 | 39·534 |
| 86-1g | 0·70331 | 0·512907 | 5·2 | 19·827 | 15·616 | 39·523 | 0·862 | 28·19 | 86·6 | 0·70326 | 5·4 | 19·707 | 15·610 | 39·406 |
| 91-1g | 0·70340 | 0·512855 | 4·2 | 20·148 | 15·661 | 39·982 | 1·47 | 36·59 | 121·4 | 0·70334 | 4·4 | 20·012 | 15·655 | 39·838 |
| 101-2g | 0·70295 | 0·513096 | 8·9 | 18·742 | 15·522 | 38·322 | 0·159 | 5·41 | 17·0 | 0·70295 | 8·7 | 18·719 | 15·521 | 38·309 |
| 103-3g | 0·70327 | 0·512907 | 5·2 | 19·722 | 15·626 | 39·461 | 1·63 | 36·24 | 116·5 | 0·70320 | 5·4 | 19·582 | 15·619 | 39·317 |
| 104-1g | 0·70319 | 0·512937 | 5·8 | 19·502 | 15·607 | 39·225 | 1·18 | 26·94 | 85·2 | 0·70314 | 6·0 | 19·401 | 15·602 | 39·123 |
| 112-1wr | 0·70543 | 0·512855 | 4·2 | 19·143 | 15·654 | 38·824 | 6·54 | 28·01 | 43·0 | 0·70541 | 4·4 | 19·041 | 15·649 | 38·774 |
| 115-1wr | 0·70367 | 0·512835 | 3·8 | 20·066 | 15·651 | 39·941 | 3·18 | 24·83 | 161·7 | 0·70365 | 4·0 | 20·003 | 15·648 | 39·811 |
| 121-1wr | 0·71002* | 0·512901 | 5·1 | 19·514 | 15·628 | 39·398 | 4·11 | 24·97 | 101·9 | 0·70713* | 5·3 | 19·440 | 15·625 | 39·301 |
| 122-1wr | 0·70341 | 0·512922 | 5·5 | 19·403 | 15·617 | 39·172 | 1·50 | 27·72 | 76·1 | 0·70338 | 5·6 | 19·327 | 15·613 | 39·106 |
| 126-1g | 0·70321 | 0·512937 | 5·8 | 19·446 | 15·617 | 39·172 | 0·788 | 30·55 | 93·8 | 0·70318 | 5·9 | 19·371 | 15·614 | 39·099 |
| 127-4g | 0·70333 | 0·512891 | 4·9 | 19·746 | 15·637 | 39·532 | 2·55 | 34·54 | 109·2 | 0·70326 | 5·0 | 19·681 | 15·634 | 39·466 |
| 129-1g | 0·70361 | 0·512850 | 4·1 | 19·908 | 15·646 | 39·734 | 1·12 | 31·34 | 128·3 | 0·70360 | 4·2 | 19·862 | 15·644 | 39·674 |
| 130-4g | 0·70270 | 0·513081 | 8·6 | 18·728 | 15·508 | 38·184 | 0·451 | 11·26 | 29·1 | 0·70270 | 8·6 | 18·709 | 15·507 | 38·169 |
| 131-1wr | 0·70336 | 0·512907 | 5·2 | 18·951 | 15·620 | 38·597 | 7·36 | 9·35 | 33·9 | 0·70336 | 5·3 | 18·936 | 15·619 | 38·579 |
| 137-2g | 0·70334 | 0·512860 | 4·3 | 19·891 | 15·634 | 39·675 | 1·73 | 32·70 | 106·1 | 0·70333 | 4·3 | 19·871 | 15·633 | 39·654 |
| 138-1g | 0·70326 | 0·512876 | 4·6 | 19·727 | 15·627 | 39·528 | 0·638 | 29·82 | 106·2 | 0·70325 | 4·6 | 19·707 | 15·626 | 39·505 |
| 139-1g | 0·70346 | 0·512866 | 4·4 | 19·751 | 15·636 | 39·626 | 2·14 | 33·39 | 104·5 | 0·70346 | 4·4 | 19·737 | 15·635 | 39·612 |
| D-58wr | 0·70426* | 0·512942 | 5·9 | 19·688 | 15·622 | 39·197 | 0·964 | 99·34 | 69·3 | 0·70424* | 6·0 | 19·355 | 15·607 | 39·123 |
| D-62wr | 0·70330 | 0·512937 | 5·8 | 19·559 | 15·609 | 39·304 | 1·60 | 29·65 | 127·1 | 0·70325 | 6·0 | 19·436 | 15·603 | 39·136 |
| D-72wr | 0·70306 | 0·512932 | 5·7 | 19·511 | 15·611 | 39·213 | 3·74 | 43·69 | 173·0 | 0·70306 | 5·7 | 19·502 | 15·611 | 39·201 |

The measured isotope ratios (subscript m) have been age-corrected (t) using data from Table 1 or, for dredge hauls with no $^{40}Ar–^{39}Ar$ dates, ages estimated from the best-fit line in Fig. 3. Fractionation corrections are 0·1194 for $^{86}Sr/^{88}Sr$ and 0·242436 for $^{148}NdO/^{144}NdO$. Data are reported relative to measured $^{87}Sr/^{86}Sr = 0·710238 \pm 0·000014$ ($2\sigma$, $n = 29$) for NBS987 Sr and to $^{143}Nd/^{144}Nd = 0·511843 \pm 0·000008$ ($2\sigma$, $n = 25$; this uncertainty corresponds to $\pm 0·2$ $\varepsilon_{Nd}$ units) for La Jolla Nd. Lead isotope ratios were measured with a double-spike method (Galer, 1999) in multi-static mode on 5–10 ng loads of sample; mean values obtained for 5–10 ng loads of NBS981 Pb were $16·938 \pm 0·003$, $15·494 \pm 0·004$, and $36·712 \pm 0·008$ ($2\sigma$, $n = 33$) for $^{206}Pb/^{204}Pb$, $^{207}Pb/^{204}Pb$, and $^{208}Pb/^{204}Pb$, respectively. Within-run errors on the isotopic data above are less than or equal to the external uncertainties on these standards. Pb concentrations were determined by isotope dilution with a relative uncertainty of 0·5%. Total procedural blanks are <40 pg for Pb, <35 pg for Sr, and <12 pg for Nd. Values of $\varepsilon_{Nd}$ are calculated assuming present bulk-Earth $^{143}Nd/^{144}Nd = 0·51264$. For DRFT 121-1, the concentrations for the leached split are Rb = 59·45 ppm, Sr = 16·69 ppm, and for GS7202-58 are Rb = 5·40 ppm, Sr = 240·8 ppm.

*$^{87}Sr/^{86}Sr$ was determined on strongly acid-leached powders for these samples and the age correction uses the Rb and Sr concentrations measured by isotope dilution.

rocks. Glass chips were cleaned ultrasonically with methanol, 1·5M HCl, and 18 MΩ cm water prior to mounting for major-element analysis or dissolution for trace element and Nd–Pb–Sr isotopic analysis. Glasses were used for most of the chemical and isotopic measurements. For the remaining samples, sawn slabs of holocrystalline rock were used. The slabs were cleaned ultrasonically in a 0·1M $HF$–$HNO_3$ solution for 5 min followed by rinsing and ultrasonically cleaning in 18MΩ cm water, to remove contamination from sawing. The dried slabs were crushed to 1–3 mm size chips, which were leached sequentially in an ultrasonic bath with cold 3M acetic acid, 3M hydrogen peroxide and 1M hydroxylamine hydrochloride to remove carbonate, phosphate, organic matter, and ferromanganese oxides (each step was interspersed with rinsing and ultrasonically cleaning in water) before being powdered for both chemical and Nd–Sr–Pb isotopic analyses. This procedure, which we have used in previous studies (e.g. Mahoney *et al.*, 2005; Ingle *et al.*, 2007), avoids the use of strong acids, to minimize disturbance of other phases in the rock. For all samples, Sr, Pb, and Nd isotopic analyses were performed using splits of the same dissolution of sample. In addition, splits of powders of two of the most visibly altered holocrystalline samples (GS7202-58, DRFT 121-1) were further subjected to a multi-step, strong-acid leaching procedure (Mahoney, 1987) for Sr isotope analysis only (also see the footnote of Table 4).

The major element contents of glass samples were determined using a Cameca SX-60 electron microprobe. A Siemens 303-AS X-ray fluorescence spectrometer was employed for holocrystalline samples. The measurements were carried out following Hall & Sinton (1996). Each electron microprobe analysis in Table 2 is an average of 6–10 'point' analyses and each X-ray fluorescence analysis is an average of two measurements of different aliquots. Trace element analyses were performed on a VG PQ-2S inductively coupled plasma–mass spectrometer, following the methods of Neal (2001). Neodymium, Sr, and double-spike Pb isotope-ratio measurements of selected samples (Table 4) were carried out on a VG Sector thermal ionization mass spectrometer at the University of Hawaii following Mahoney *et al.* (1994, 2005) and Galer (1999). Age-corrected values in Table 4 were calculated using parent and daughter element concentrations (Table 3 for Sm, Nd, Rb, Sr, U, and Th, and Table 4 for Pb) measured on splits of the same sample powders used for isotopic analysis. For age-correcting the Sr isotope ratios of the strongly leached splits of GS7202-58 and DRFT 121-1, the concentrations of Sr and Rb were determined by isotope dilution (see the Table 4 legend for the values).

## RESULTS

### $^{40}Ar$–$^{39}Ar$ ages of lavas

Thirty-two of the 40 NR and ESC dredged rocks yielded acceptable $^{40}Ar$–$^{39}Ar$ plateau or isochron ages (Table 2). These samples included whole-rocks and groundmass and plagioclase separates. Figures 2 and 3 show a selection of step-heating apparent-age spectra. In general, samples produced good plateaux comprising 90–100% of the total gas, and we regard these as reliable estimates of the sample crystallization age. Corresponding isochron ages are concordant and have $^{40}Ar/^{36}Ar$ intercepts within error of the atmospheric value. The age spectra for several whole-rock and groundmass samples reveal the effects of recoil (re-location of $^{37}Ar$ and $^{39}Ar$ atoms during neutron irradiation), characterized by decreasing step age with increasing heating temperature (e.g. sample DM14-1028-11 in Fig. 3). In these cases the best estimate of crystallization age is the total fusion age (in italics in Table 2), calculated by summing all steps.

The youngest sample, GS7202-72-2, is from the submarine slope of Salas y Gomez, whereas the oldest ages (29·9 ± 0·3 Ma and 30·8 ± 0·8 Ma) are for samples from one of the two easternmost dredge sites on the NR (GS7202-62; Fig. 1). There is a clear, overall linear trend of increasing age eastward from Salas y Gomez, except for two samples (DRFT 84-1 and 85-1) from an NR seamount with plateau ages of 4·5 Ma and 5·0 Ma in the midst of seamounts with ages older than 24 Ma (Table 2). These anomalously young lavas thus are not related to the volcanism that produced the rest of the NR; they will be discussed further in subsequent sections. We fitted the age distributions of the ESC and NR seamounts with linear regressions (Fig. 4), which indicate that the age of the 'elbow' in the NR–ESC system, where the NR meets the ESC, is 23 ± 1 Ma. This age corresponds to a change in Pacific plate motion estimated at about 23 Ma by Wessel & Kroenke (2000) and may reflect the breakup of the Farallon plate into the Nazca and Cocos plate pair (e.g. Barckhausen *et al.*, 2008).

### Major and trace element geochemistry

The majority of the lavas are moderately evolved, transitional to moderately alkalic basalts ($MgO = 4$–$7$ wt %, $TiO_2 = 2$–$4$ wt %, $K_2O = 0{\cdot}5$–$1{\cdot}65$ wt %). However, a few tholeiitic (DRFT 101-2 and 130-1, 130-4, and 130-5), more alkali-rich ($Na_2O + K_2O > 5{\cdot}5$ wt %; DRFT 84-1, 85-1, 115-1, 135-6, and GS7202-DR72-2), and more siliceous compositions (particularly DRFT 121-1, a trachyte with 64·50 wt % $SiO_2$) are also present (Fig. 5a). Two of the most alkalic samples, a tephrite and a foidite (DRFT 84-1 and 85-1), are the anomalously young NR samples mentioned above; it is not clear whether they represent an anomalously young seamount or instead some sort of rejuvenated volcanism on a much older (>24 Ma) seamount. Four samples have $MgO > 8$ wt %; three are tholeiites and one is the tephrite, which is holocrystalline. All four of these samples contain olivine phenocrysts. Overall, Mg# [$= 100 \times Mg^{2+}/(Mg^{2+} + Fe^{2+})$, molar, assuming 85% of total iron is $Fe^{2+}$] varies from 65 to 42, with a

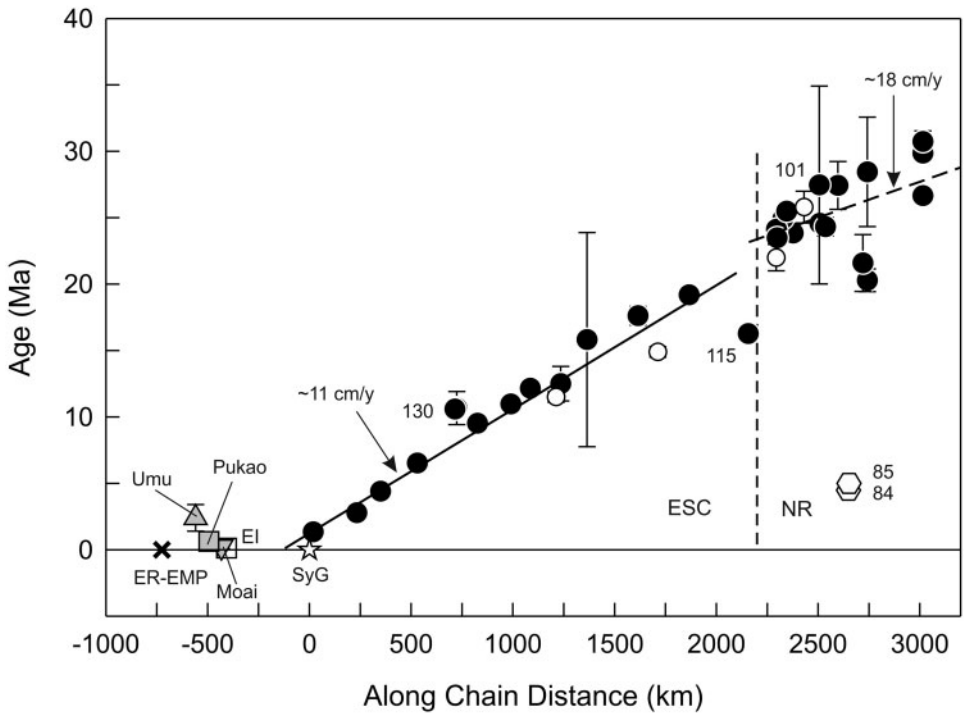


**Fig. 4.** Distribution of $^{40}Ar-^{39}Ar$ ages of NR, ESC and Easter Island (EI) volcanic rocks vs along-chain distance from Salas y Gomez (SyG). Also shown are the data for lava fields and small seamounts west of EI. Lavas of the East Rift of the Easter Microplate (ER-EMP) are assigned an age of 0 Ma. Our data (plateau ages for all samples from Table 2 except the total fusion age for DRFT 100-2 and isochron ages for DRFT 115-2 and 126-1) are indicated by filled circles and, for two anomalously young NR samples (DRFT 84-1 and 85-1), by hexagons. Open circles and other symbols are data from O'Connor *et al.* (1995). Error bars indicate $\pm 2\sigma$ uncertainties on age, if larger than the size of the symbol. The inclined continuous and dashed lines represent linear regressions performed using the algorithm of York *et al.* (2004) on data for the ESC and NR, respectively, considering the $2\sigma$ errors on age (years) only (i.e. assuming no significant error resides in the dredge-site locations). Data for the anomalously young DRFT 84 and 85 samples, EI, and seamounts and lava fields west of it are not included in the regressions. These regressions equate to plate motion speeds of $18 \pm 1$ and $10{\cdot}7 \pm 0{\cdot}1\,cm\,a^{-1}$ during the formation of the NR and ESC, respectively. The dashed vertical line roughly marks the boundary between the NR and ESC.

mode around 55, reflecting the rather evolved nature of most of the lavas. No systematic relationship is apparent between rock composition and sampling location on a seamount (e.g. upper portion vs lower flanks). From these results, it appears possible that the majority of the ESC and NR volcanoes may not have passed through compositionally distinct shield, postshield, and rejuvenated stages, in contrast to Hawaiian volcanoes, and instead may be more similar to the volcanoes of, for example, the Louisville chain (Beier *et al.*, 2011; Expedition 330 Scientists, 2011). Alternatively, our sampling may have largely failed to retrieve such rocks (but see below).

Despite our efforts to avoid and remove alteration during sample preparation, significant alteration effects are evident in the chemical analyses of two bulk-rocks and one glass. These samples (DRFT 112-1, DRFT 130-5, GS7202-58) all contain abundant secondary phosphate, and one of the most notable chemical characteristics in the processed splits is the markedly high P content relative to concentrations of elements of similar incompatibility, such as Nd and Zr. In addition, some combination of high U relative to Th and Nb (DRFT 112-1, GS7202-58), high K relative to Th and Nb (DRFT 130-5, GS7202-58), and/or low $Na_2O$ for a given MgO content (DRFT 112-1, GS7202-58; Fig. 5f) is present. Sample DRFT 112-1 also has a distinctly high Pb content relative to Nd, Pr, and Ce. Relative enrichment in Pb is even greater in another bulk-rock sample, DRFT 131-1, which exhibits only modest enrichment in $P_2O_5$. Two other bulk-rock samples, phonotephrite DRFT 115-1 and basalt DRFT 127-1, have low U relative to Th and Nb, ($Th/U = 6{\cdot}30$ and $6{\cdot}45$, respectively); this may be an alteration effect from a subaerial stage of weathering or a result of our sample cleaning and leaching procedure. We do not rely on the data for these elements in any of this group of samples in the discussion and interpretations that follow.

Even though the rocks range from alkalic to tholeiitic, the data define moderate correlations of MgO with CaO, $Na_2O$, $K_2O$, $SiO_2$, and $CaO/Al_2O_3$ if the foidite and tephrite, as well as the altered samples noted above, are excluded (Fig. 5b, c, d, f). In general, the correlations are consistent with removal of variable amounts of olivine,

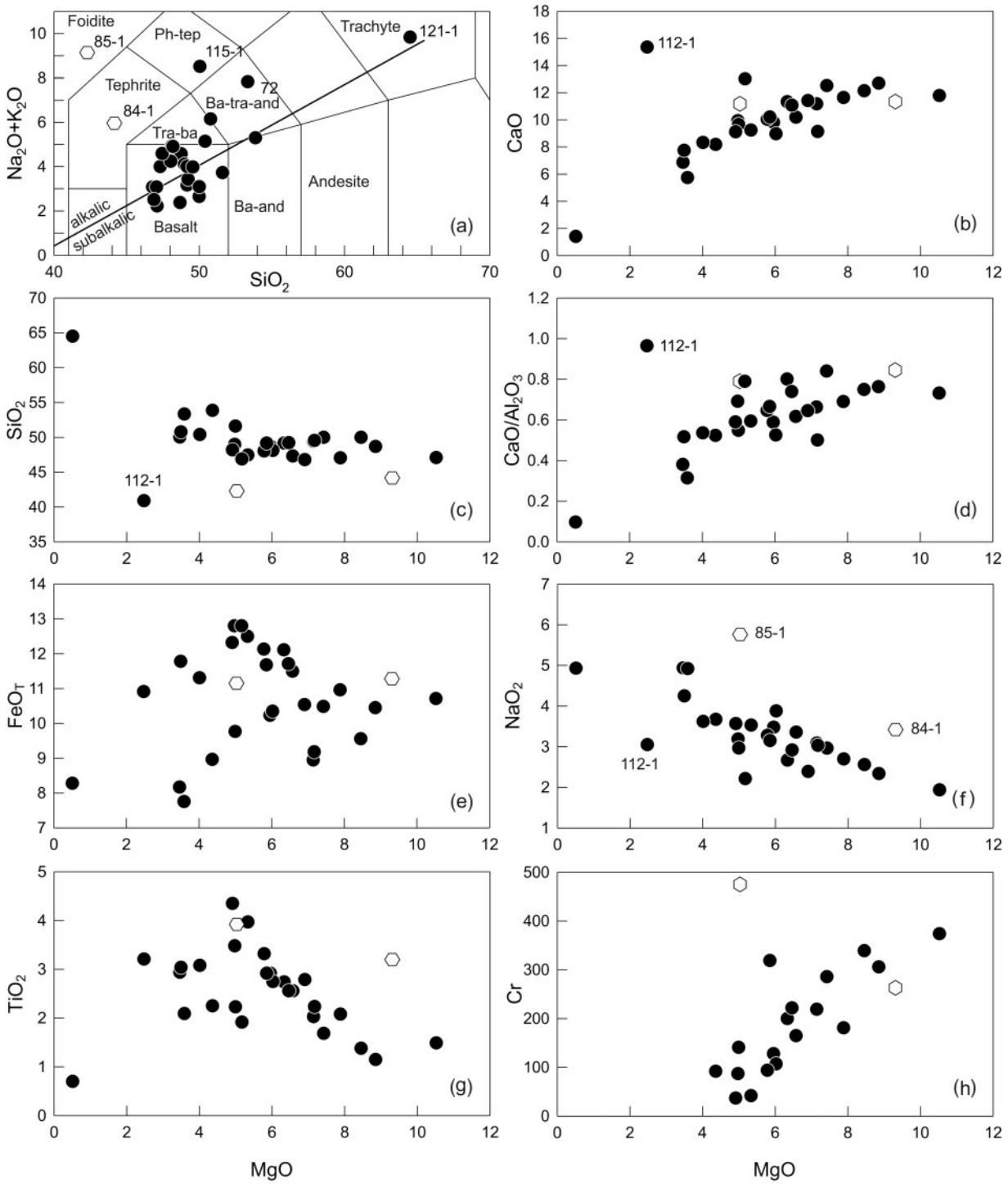


**Fig. 5.** (a) Total alkalis vs silica (wt %) for glass and holocrystalline samples. The fields are from Le Maitre (1989), and the boundary between sub-alkalic and alkalic compositions for Hawaiian lavas is from Macdonald & Katsura (1964). Samples with compositions outside the field for basalt are labeled. Data for tephrite DRFT 84-1 and foidite DRFT 85-1 from the young NR seamount are shown with hexagons. Ba-and, basaltic andesite; Tra-ba, trachybasalt; Ba-tra-and, basaltic trachyandesite; Ph-tep, phonotephrite. (b–h) MgO vs selected major element oxides (wt %) and Cr (ppm). Data points for altered samples lying off-trend are labeled in relevant panels.

clinopyroxene, and plagioclase during magmatic differentiation. $TiO_2$ correlates negatively with MgO at MgO values greater than about 5 wt % (Fig. 5g), but the correlation disappears at lower MgO values, suggestive of varying amounts of Fe–Ti oxide mineral removal. A rough negative correlation is also seen for $P_2O_5$ vs MgO, with the exception of the trachyte, DRFT 121-1; the very low $P_2O_5$ (0·05 wt % at MgO of 0·51 wt %) of this evolved lava is consistent with apatite removal. Total iron as FeO ($FeO^T$; Fig. 5e) and $Al_2O_3$ do not correlate significantly with MgO but exhibit a spread of values at a given MgO content. Pan & Batiza (1998) interpreted a similar result for ESC lavas west of Salas y Gomez as evidence for a range of mean pressures of fractionation and melting. Incompatible trace elements (Rb, Nb, Sm, Zr, etc.) display no or very crude negative correlations with MgO, whereas compatible trace elements (Ni, Cr, Co, and to a lesser extent, Sc; e.g. Fig. 5h) define somewhat better positive correlations.

The major oxide variations of the transitional and alkalic basalts are similar to those observed for ESC lavas west of Salas y Gomez (Haase & Devey, 1996; Haase *et al.*, 1997; Pan & Batiza, 1998). As with the more westerly lavas, the $Na_2O$, $Al_2O_3$, and K/Ti values of our samples are generally higher at a given MgO content than those in basalts of the southern EPR and rifts of the Easter Microplate. For glass samples with MgO > 5·5 wt %, Fig. 6 compares values of $Na_2O$, $SiO_2$, and $CaO/Al_2O_3$ adjusted to 8 wt % MgO to minimize effects of variable shallow-level differentiation. Most of our samples from the NR and ESC east of Salas y Gomez are like the majority of those from the ESC west of Salas y Gomez in having comparatively low $(CaO/Al_2O_3)_8$ and $(SiO_2)_8$ for a given value of $(Na_2O)_8$ [also, values of $(FeO^T)_8$ tend to be higher, but the lack of correlation of $FeO^T$ with MgO makes the calculation and interpretation of $(FeO^T)_8$ problematic for these samples]. These differences are consistent with smaller average amounts of partial melting and greater average depths of melting for lavas of the NR and ESC east of Salas y Gomez than for basalts of the southern EPR and rifts of the Easter Microplate. We return to this subject below.

Figure 7 shows representative primitive-mantle-normalized incompatible element patterns, along with average patterns for ocean island basalts (OIB) and normal and incompatible-element-enriched mid-ocean ridge basalts (N- and E-MORB, respectively). For clarity, the patterns of the samples have been divided into four groups on the basis of dredge location. The DRFT 101 and 130 tholeiites exhibit patterns similar to those of N-MORB, with relative depletion in the highly incompatible elements [e.g. primitive-mantle-normalized $(La/Lu)_p = 0·35$ in DRFT 101-2], but all the other lavas are relatively enriched in the highly incompatible elements, similar to typical OIB or E-MORB [most have $(La/Lu)_p$ between 1·7 and 9·2; the DRFT 85-1 foidite has a value of 26]. The lavas generally show the greatest relative enrichment at Nb and Ta, a characteristic of many OIB. Troughs at Ti (e.g. DRFT 85-1, 121-1, 135-4, and GS7202-72-2), P (e.g. DRFT 121-1, 127-1 and 127-4), and Sr (e.g. DRFT 121-1, 127-1, 127-4, and 135-4) in several patterns are indicative of significant oxide mineral, apatite, and plagioclase control, respectively.

The most pronounced troughs at P, Ti, and Sr are seen for the trachyte, DRFT 121-1 (Fig. 7b). This evolved sample also has the highest weight loss-on-ignition measured for any of our samples (6·07 wt %), yet its incompatible-element pattern lacks the distinctive characteristics of other altered samples, such as DRFT 112-1. Instead, unlike any of our other samples, the DRFT 121-1 pattern has a sizeable trough at Ba. A Ba trough can be produced by fractional crystallization of potassium feldspar, in which Ba is compatible (e.g. Green, 1994). However, this would also deplete K; yet the pattern lacks a K trough. We have no good explanation at present for the Ba trough (although we can speculate that K added during alteration of the sample obscures what would otherwise be a K trough).

Correlations among ratios of incompatible elements are similar to those found by previous workers for the ESC west of Salas y Gomez (Fig. 8a–d), but show somewhat more scatter for some ratios, principally those involving the more alteration-sensitive elements in the bulk-rock samples (e.g. U in Nb/U, Fig. 8c). In common with results for many other hotspots, nearly all of our data fall within the field of Nb/Y vs Zr/Y defined by lavas of the Icelandic hotspot (Fig. 8d). The only exceptions are the N-MORB-like tholeiitic basalts (DRFT 101-2 and three DRFT 130 samples), whose values lie below this field within the range of N-MORB. Data for two seamounts west of Easter Island (Haase & Devey, 1996) and an Easter Island rhyolite (Haase *et al.*, 1997) also lie significantly below the Iceland field.

An important difference between our samples and lavas of the ESC west of Salas y Gomez is that our data show no overall correlation of chemical characteristics with seamount location (Fig. 9a–f). This result contrasts with the systematic along-chain trends seen between the East Rift and Salas y Gomez (Haase & Devey, 1996; Pan & Batiza, 1998; Kingsley *et al.*, 2007).

## Sr–Nd–Pb isotope ratios

Figure 10 compares our age-corrected Sr–Nd–Pb isotopic data with previously published data for the ESC, southern EPR, and the young (*c.* 0·4 Ma; Haase *et al.*, 2000) islands of San Felix and San Ambrosio, which lie about 200 km SE of the ~23 Ma 'elbow' in the ESC–NR system. In Fig. 11, we compare the age-corrected Nd–Pb isotopic data from the ESC and NR with those for the islands of

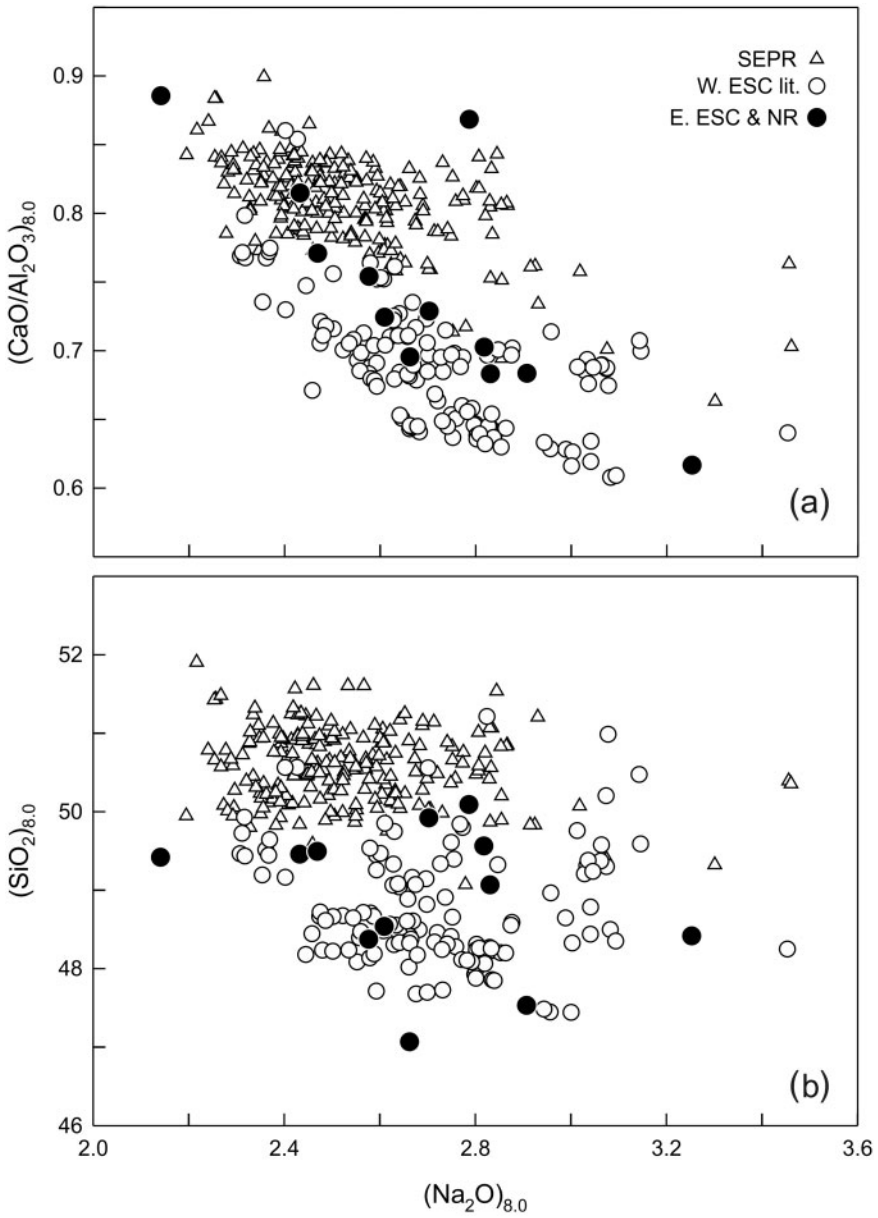


**Fig. 6.** Variation of $(Na_2O)_8$ vs (a) $(CaO/Al_2O_3)_8$ and (b) $(SiO_2)_8$ for glass samples with MgO > 5·5 wt %. Adjustment to 8 wt % MgO followed the method of Klein & Langmuir (1987). 'E. ESC & NR' indicates our data. Other data sources: southern East Pacific Rise (SEPR): Sinton *et al.* (1991), Hékinian *et al.* (1992, 1995), Hall & Sinton (1996) and Niu & Hékinian (1997); ESC west of Salas y Gomez Ridge (W. ESC lit.): Haase & Devey (1996) and Pan & Batiza (1998).

Hawaii and Samoa, two primary hotspots of the Pacific plate. The different isotope ratios correlate strongly overall, and the total range exhibited by our data [$\varepsilon_{Nd}(t) = +8{\cdot}7$ to $+2{\cdot}9$, $(^{206}Pb/^{204}Pb)_t = 18{\cdot}709$–$20{\cdot}012$ and, with three exceptions, $(^{87}Sr/^{86}Sr)_t = 0{\cdot}70270$–$0{\cdot}70388$] is similar to the previously measured ESC range, which is defined almost completely by <2 Ma lavas west of Salas y Gomez. However, data for the great majority of our samples cluster in a much smaller field between age-corrected $\varepsilon_{Nd}(t)$ of $+6{\cdot}0$ and $+4{\cdot}0$, $(^{87}Sr/^{86}Sr)_t$ of 0·70306 and 0·70365, and $(^{206}Pb/^{204}Pb)_t$ of 19·327 and 20·012. Variation in $^{207}Pb/^{204}Pb$ relative to $^{206}Pb/^{204}Pb$ for this group of samples is less than observed in previous ESC data, which we attribute to our use of a double-spike method for determination of Pb isotope ratios. Data for this group of samples lie in the isotopic range of proposed 'common' or 'C-type' mantle (Hanan & Graham, 1996) and recently redefined 'focus zone' or 'FOZO-type' mantle (Stracke *et al.*, 2005).

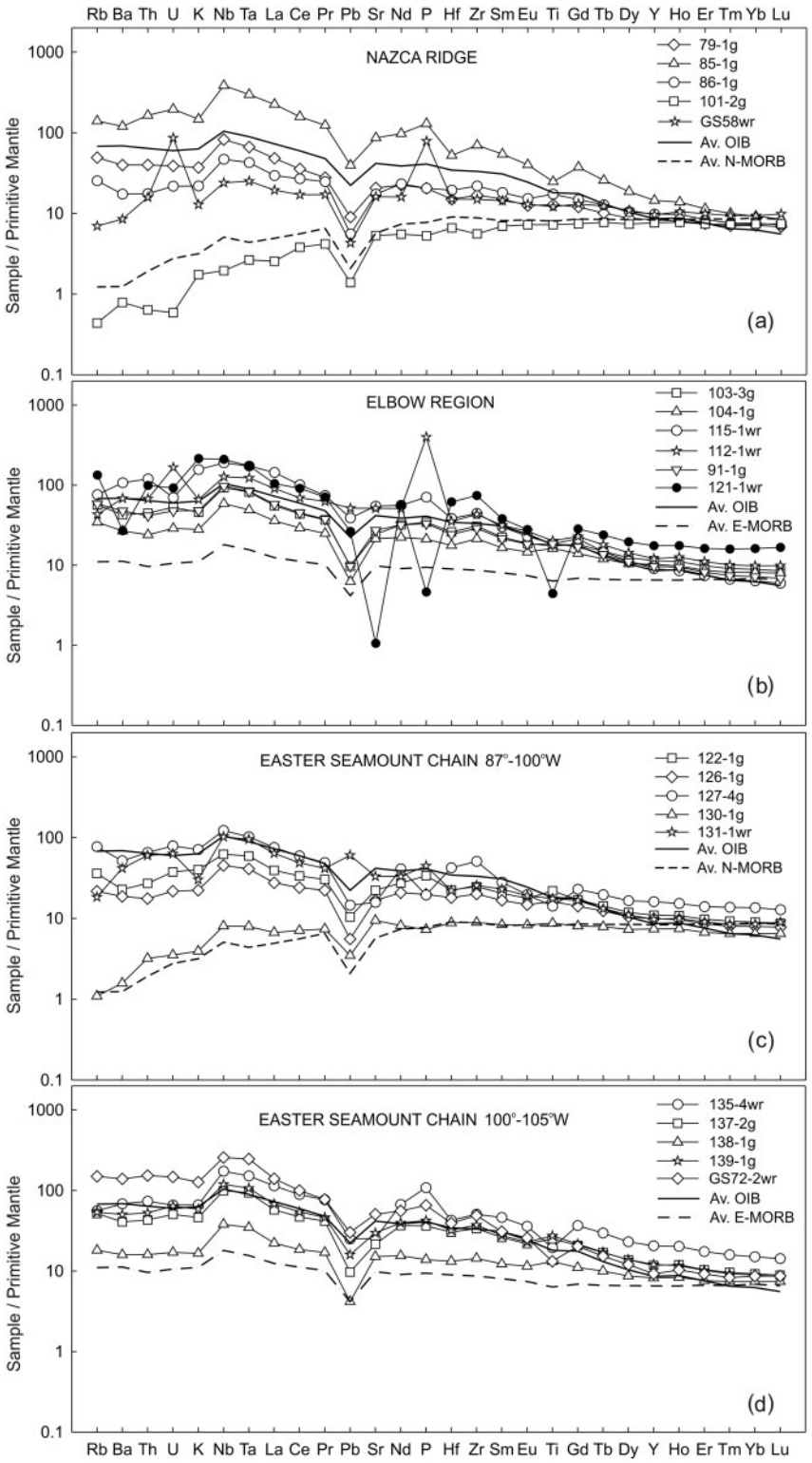


**Fig. 7.** Primitive-mantle-normalized incompatible element patterns of representative samples from different portions of the NR and ESC. Normalizing values are from Lyubetskaya & Korenaga (2007); global average N-MORB, E-MORB and OIB patterns are from Sun & McDonough (1989).

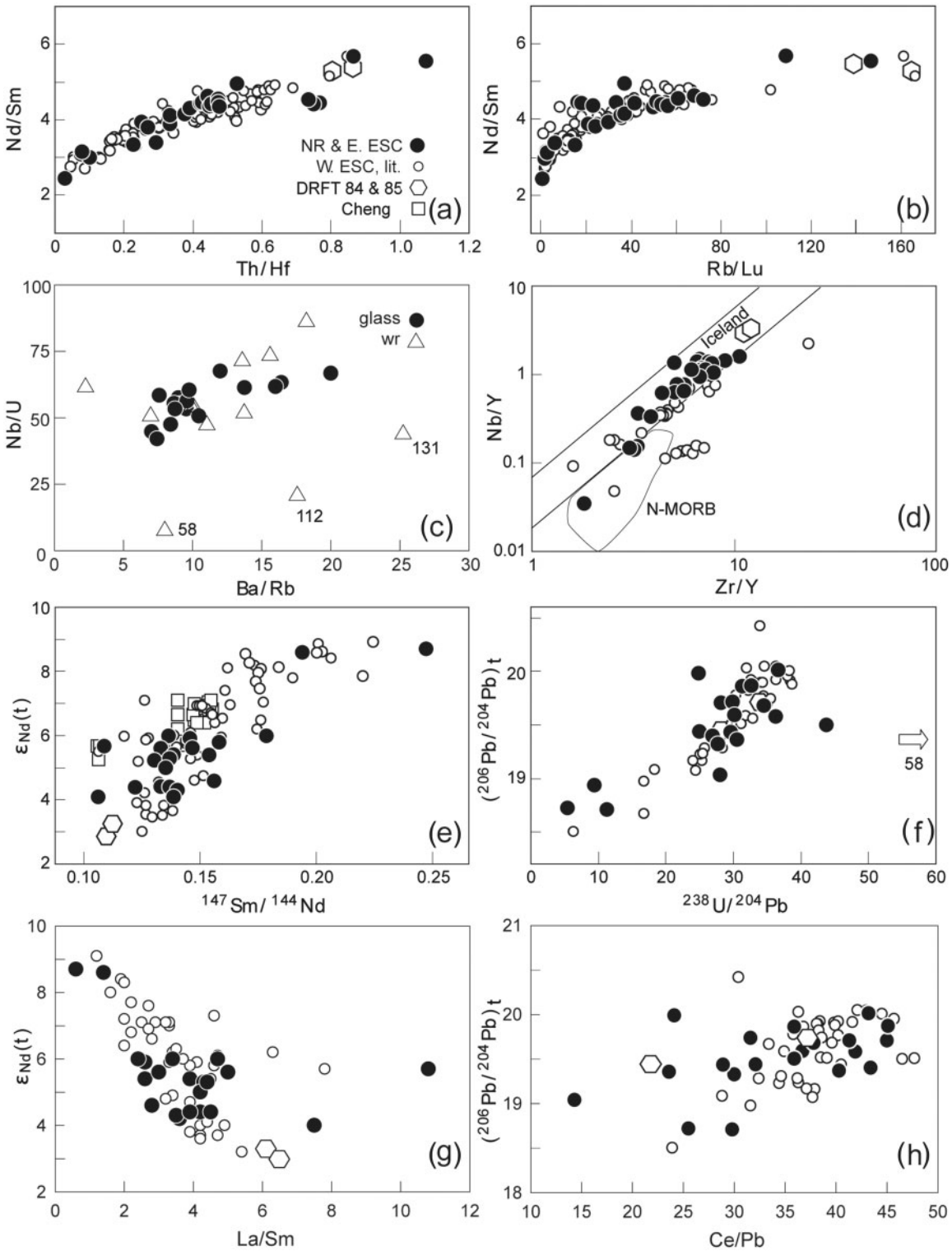


**Fig. 8.** Nd/Sm vs (a) Th/Hf and (b) Rb/Lu; (c) Nb/U vs Ba/Rb; (d) Nb/Y vs Zr/Y; (e) $\varepsilon_{Nd}(t)$ vs $^{147}Sm/^{144}Nd$; (f) $(^{206}Pb/^{204}Pb)_t$ vs $^{238}U/^{204}Pb$; (g) $\varepsilon_{Nd}(t)$ vs La/Sm; (h) $(^{206}Pb/^{204}Pb)_t$ vs Ce/Pb. 'NR & E. ESC' and 'DRFT 84 & 85' are data from this study; 'W. ESC, lit.' indicates data from the literature for the ESC west of Salas y Gomez (Haase *et al.*, 1996, 1997; Haase & Devey, 1996) and 'Cheng' indicates the data of Cheng *et al.* (1999). Element ratios in (a), (b) and (d) were chosen to include elements analyzed in common by different workers, whereas in (c) only data for our NR & E. ESC glass and whole-rock (wr) samples are plotted. Fields for Iceland and N-MORB in (d) are from Fitton (2007).

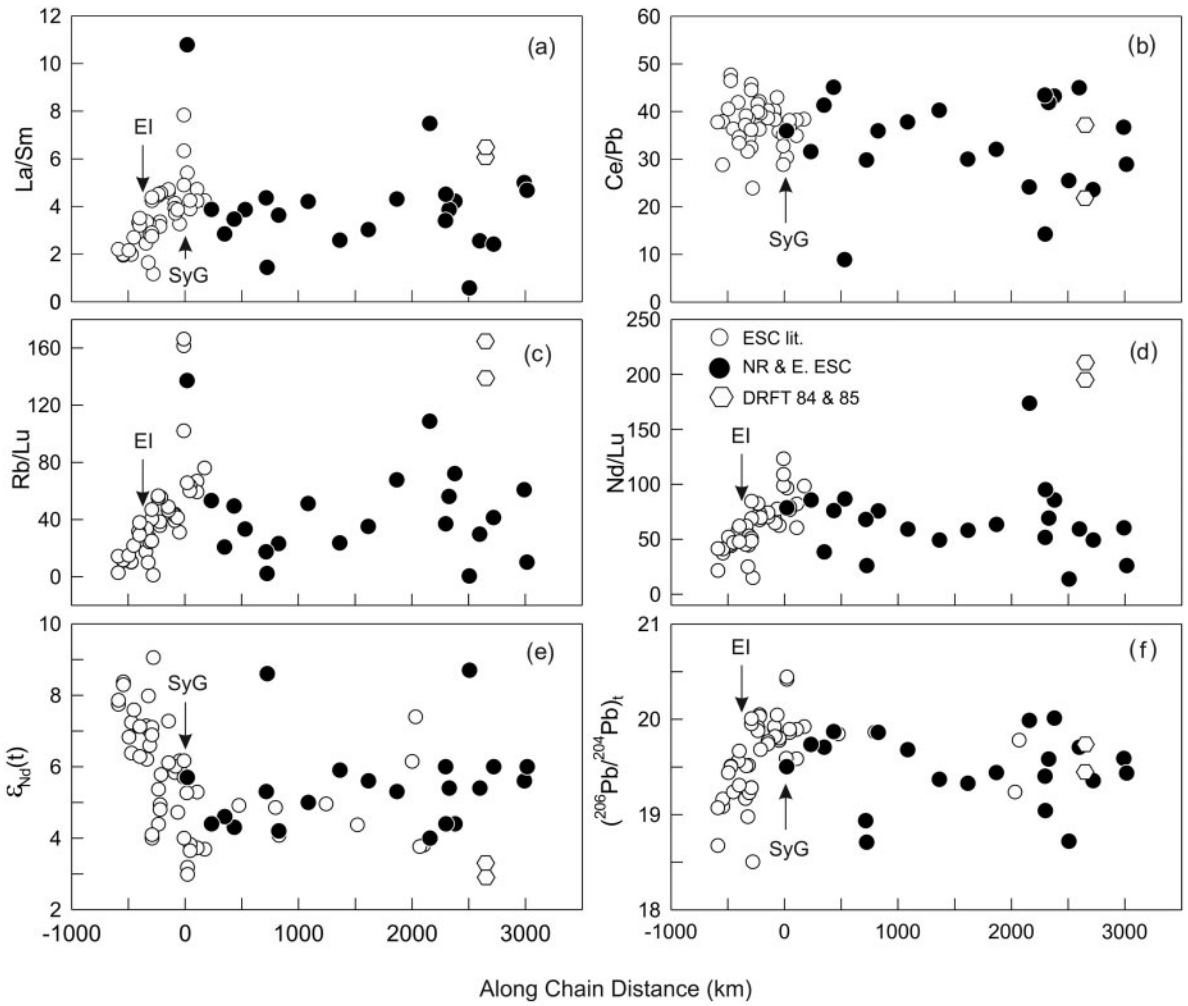


**Fig. 9.** Trace element (a–d) and isotopic ratios (e, f) vs along chain distance (great circle) from SyG. Data sources are as for Fig. 8.

Globally, such mantle is abundant in both ocean island and ocean ridge sources. It is usually attributed to aged, recycled, subducted oceanic crustal material present in both mantle plumes and non-plume upper mantle. However, as Kingsley *et al.* (2007) noted, the highest $^{206}Pb/^{204}Pb$ values seen in the Easter–Salas hotspot system are slightly greater than the maximum proposed for C or FOZO. Nevertheless, it is clear that the low-$\varepsilon_{Nd}$, high-$^{206}Pb/^{204}Pb$ material in the Easter–Salas system is broadly C/FOZO-like.

Isotopic effects of alteration are pronounced in four holocrystalline samples. Three of these, GS7202-58, DRFT 112-1, and the trachyte, DRFT 121-1, have anomalously elevated $(^{87}Sr/^{86}Sr)_t$ relative to their $\varepsilon_{Nd}(t)$ values, placing their data points far off the main array in Fig. 10a (note that this is despite the strong acid-leaching of the splits of GS7202-58 and DRFT 121-1 analyzed for Sr isotopes). The trachyte has the highest $(^{87}Sr/^{86}Sr)_t$ [0·70713, at $\varepsilon_{Nd}(t) = +5{\cdot}3$] and also the lowest Sr concentration of any of our samples; this lava contains only 17 ppm Sr, or only about twice the concentration of seawater (~8 ppm; e.g. Li, 1991), making its Sr isotope ratio particularly sensitive to seawater alteration. Samples DRFT 112-1 and DRFT 131-1, both of which show marked relative enrichment in Pb (see previous section), have high $(^{207}Pb/^{204}Pb)_t$ for their $(^{206}Pb/^{204}Pb)_t$; also, their $(^{206}Pb/^{204}Pb)_t$ values (19·041, 18·936) are lower than those of other samples with similar $\varepsilon_{Nd}(t)$ (Fig. 10b and c). As with the concentration data for the alteration-sensitive elements, we do not use the Sr or Pb isotope ratios of this group of samples in our interpretations or in subsequent figures.

Values for the two chemically N-MORB-type tholeiitic basalts that we analyzed isotopically (DRFT 101-2 and 130-4) lie far from the main isotopic cluster, at higher $\varepsilon_{Nd}(t)$ (+8·7, +8·6) and lower $(^{87}Sr/^{86}Sr)_t$ (0·70295, 0·70270) and $(^{206}Pb/^{204}Pb)_t$ (18·719, 18·709). In Fig. 10, they fall at the low-$\varepsilon_{Nd}$ end of the southern EPR array

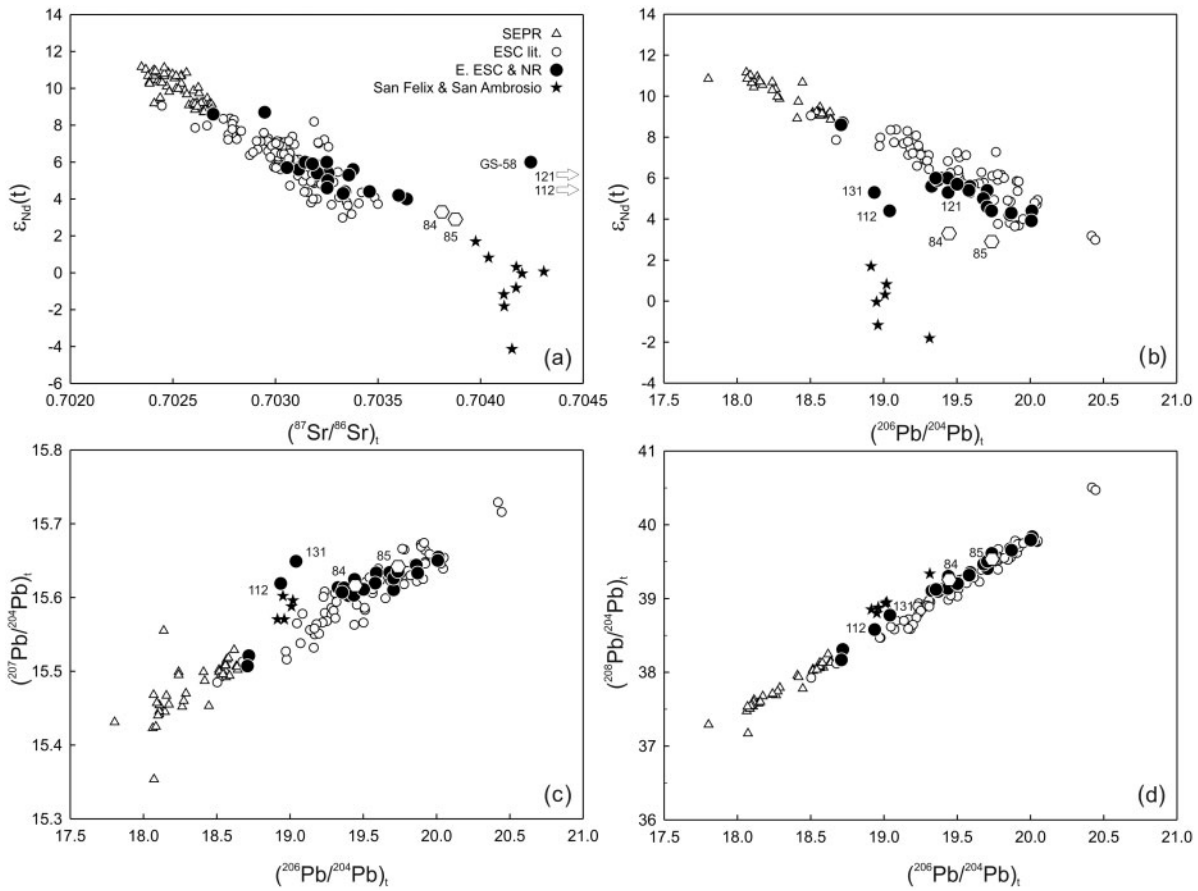


**Fig. 10.** Age-corrected Nd–Sr–Pb isotopic data. Errors on our data (E. ESC & NR) are smaller than or similar to the size of the symbols. Also shown are data for the southern East Pacific Rise (SEPR), literature data for the western ESC and Salas y Gomez Ridge (ESC lit.), and the islands of San Felix and San Ambrosio. Data sources: Gerlach *et al.* (1986); Macdougall & Lugmair (1986); White *et al.* (1987); Hanan & Schilling (1989); Fontignie & Schilling (1991); Bach *et al.* (1994); Mahoney *et al.* (1994); Haase *et al.* (1996, 2000); Schiano *et al.* (1997); Kingsley & Schilling (1998); Cheng *et al.* (1999); Haase (2002); Kingsley *et al.* (2007). All values are normalized relative to our measured isotopic ratios for standards.

and close to the high-$\varepsilon_{Nd}(t)$, low-$(^{87}Sr/^{86}Sr)_t$, low-$(^{206}Pb/^{204}Pb)_t$ extreme of previous ESC data (defined by lavas closest to the East Rift of the Easter Microplate). Data for the young NR tephrite and foidite (DRFT 84-1 and 85-1) also lie outside the main data cluster, but at higher $(^{87}Sr/^{86}Sr)_t$ (0·70381, 0·70388) and lower $\varepsilon_{Nd}(t)$ (+3·3, +2·9); in Fig. 10a and b, they are displaced toward the field of San Felix and San Ambrosio.

Correlations of isotope ratios with incompatible element ratios are generally similar to those observed for the young ESC lavas west of Salas y Gomez, except for alteration-sensitive elements and isotopes of samples showing significant alteration effects (Fig. 8e–h). If the correlations of Nd and Pb isotope ratios with their respective parent–daughter ratios (Fig. 8e and f) are interpreted as mantle errorchrons, they suggest 'ages' ranging from ~200 to 490 Ma. In contrast, the data are scattered in a plot of $(^{87}Sr/^{86}Sr)_t$ vs $^{87}Rb/^{86}Sr$, probably largely reflecting the variable influence of plagioclase (in which Sr is compatible) during magma genesis, as well as alteration effects on several samples. The $(^{207}Pb/^{204}Pb)_t$ vs $(^{206}Pb/^{204}Pb)_t$ array, if interpreted as an errorchron, yields an 'age' of about 1·7 Ga. Broadly similar results have been found in oceanic lavas elsewhere. They may have specific age significance in some cases, but are generally thought to correspond only to a rough mean evolution or 'recycling' time of source mantle with a long open-system history, or to have no real chronological significance (e.g. Dosso *et al.*, 1999; Albarède, 2001; Mahoney *et al.*, 2002).

Finally, as with their chemical characteristics, the isotopic ratios of our samples do not show any simple variation with distance along the ESC and NR (Fig. 9e and f). Again, this result contrasts with the overall west–east gradients observed along the chain west of Salas y Gomez (e.g. Haase *et al.*, 1996; Cheng *et al.*, 1999; Kingsley *et al.*, 2007). There is also no correlation of isotopic or

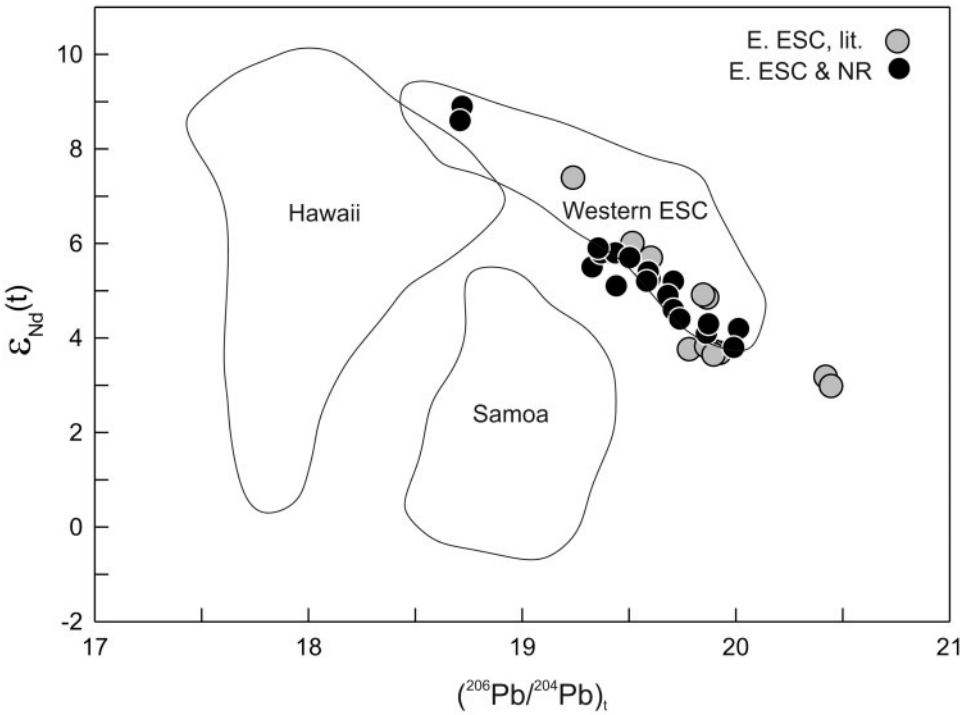


**Fig. 11.** $\varepsilon_{Nd}(t)$ vs $(^{206}Pb/^{204}Pb)_t$ for our samples (E. ESC & NR) compared with data from the literature (lit.) for the eastern ESC, and with fields for the western ESC and Hawaiian–Emperor and Samoan chains. Data for our four highly altered samples (see text) and the young NR seamount are not shown. Literature sources for ESC and NR data: Haase *et al.* (1996); Kingsley & Schilling (1998); Cheng *et al.* (1999); Kingsley *et al.* (2007). The Hawaiian–Emperor and Samoan fields were constructed with compiled data from http://www.petdb.org/ and Regelous *et al.* (2003).

incompatible element composition with sample age; however, crude correlations exist with the estimated age of the crust at the time of volcanism (see below).

## DISCUSSION

### Age and location of the Easter–Salas Hotspot

Although younger ages have been reported for Easter Island (as young as 0·13 Ma) than for Salas y Gomez (1·4 Ma), O'Connor *et al.* (1995) concluded that their age data were most compatible with a hotspot centered at Salas y Gomez. Our results show a robust, overall linear relationship between the $^{40}Ar-^{39}Ar$ ages of the seamounts along the NR and ESC east of Salas y Gomez and the along-chain distance (great circle) of these seamounts from Salas y Gomez. This age progression confirms that the ESC and NR belong to a single hotspot chain, and predicts the hotspot to be located at present between Easter Island and Salas y Gomez, but nearer the latter. Furthermore, it is clear that the hotspot has been active for more than 30 Myr, because the NR extends more than 500 km to the NE beyond the dredge site that yielded the oldest dated lavas (site GS7202-62; see Fig. 1). Even older portions of the NR may have existed but were subducted beneath South America (Espurt *et al.*, 2007). In contrast, passage of the Nazca plate over the Salas–Easter hotspot clearly did not produce the ~5 Ma lavas sampled in the DRFT 84 and 85 dredge hauls. Rather, we suspect that this highly alkalic volcanism may have been triggered by extensional stresses within the Nazca plate associated with a change in Pacific plate motion that began at about 6 Ma (Wessel & Kroenke, 2007). Around the same time, spreading ceased on the Galápagos Rise to the north of the ESC and the Nazca plate captured the Bauer microplate (e.g. Eakins & Lonsdale, 2005).

If a linear regression is performed with the combined eastern ESC and NR data in Fig. 4, including those for Salas y Gomez (SyG in the figure), then the slope of the line suggests an average speed of $10{\cdot}7 \pm 0{\cdot}1\,cma^{-1}$ ($r^2 = 0{\cdot}96$) for the Nazca plate relative to the hotspot, which is not very different from the present-day half-spreading rate for the southern EPR just north of the Easter Microplate, determined from digital models (9–10 $cma^{-1}$; Müller *et al.*, 2008). The error on the speed ($2\sigma$) is determined by propagating the error on the slope. A similar exercise for only the ESC data yields an identical average Nazca plate speed of $10{\cdot}7 \pm 0{\cdot}1\,cma^{-1}$ ($r^2 = 0{\cdot}94$). A regression for just the NR data gives a value of $18 \pm 1\,cma^{-1}$ ($r^2 = 0{\cdot}52$), which suggests a significantly

higher average speed for the plate during the early history of the NR–ESC system. The age of the NR near the trench is estimated to be 31 ±1 Ma and, as noted above, that of the NR–ESC bend or elbow at ~2200 km east of Salas y Gomez (near dredge DRFT 115; Fig. 4) is estimated to be 23 ±1 Ma. If true, the ~23 Ma elbow in the hotspot trail would correspond to a change in both the speed of the Nazca plate relative to the hotspot and the direction of plate movement. Moreover, the southwestern portion of the NR is relatively wide (Fig. 1) and ages across the NR near the elbow are similar, implying that volcanic activity was spread out over a rather wide area shortly before the change, at about 22–27 Ma. Also, it should be noted that the linear progression along the NR and ESC is not consistent either with a 'mantle hot line' (Bonatti *et al.*, 1977) or with any of the fracture propagation models.

Ages for the N-MORB-like tholeiitic samples DRFT 130-2 and 101-1 both lie ~2·5 Myr above the respective regression lines (although the uncertainty on the DRFT 101-1 age is large). Given their marked compositional differences from our other samples, it is possible that they represent an otherwise unsampled, compositionally distinct early (preshield?) stage of volcanism. Likewise, the phonotephrite DRFT 115-1 plots ~5 Myr below the regression line for the ESC; together with its unusual composition, this may indicate that it represents a postshield-stage lava.

In contrast to results for samples collected east of Salas y Gomez, lavas west of Salas y Gomez do not show an overall age progression with distance but instead indicate a rather extensive zone of recent volcanism. We suspect the same may have been true in earlier times, and may account for some of the scatter about the ESC and NR regressions in Fig. 4. However, our preference for dredge sites on the flanks of major seamounts meant that we tended to avoid low-lying features (like the recent Umu, Pukao, and Moai lava fields), many of which, in any case, would have been buried by later seamount flows as they drifted over the hotspot's center.

The age of the oceanic crust underlying a seamount can be estimated from the age of nearby seafloor magnetic anomalies (Wilder, 2003; Müller *et al.*, 2008). The difference between this age and the age of a sample gives an estimate of the age of the crust at the time of volcanism ($\Delta_{age}$ in Fig. 12 and Table 2). From this estimate and a sufficient understanding of events at the Nazca–Pacific spreading

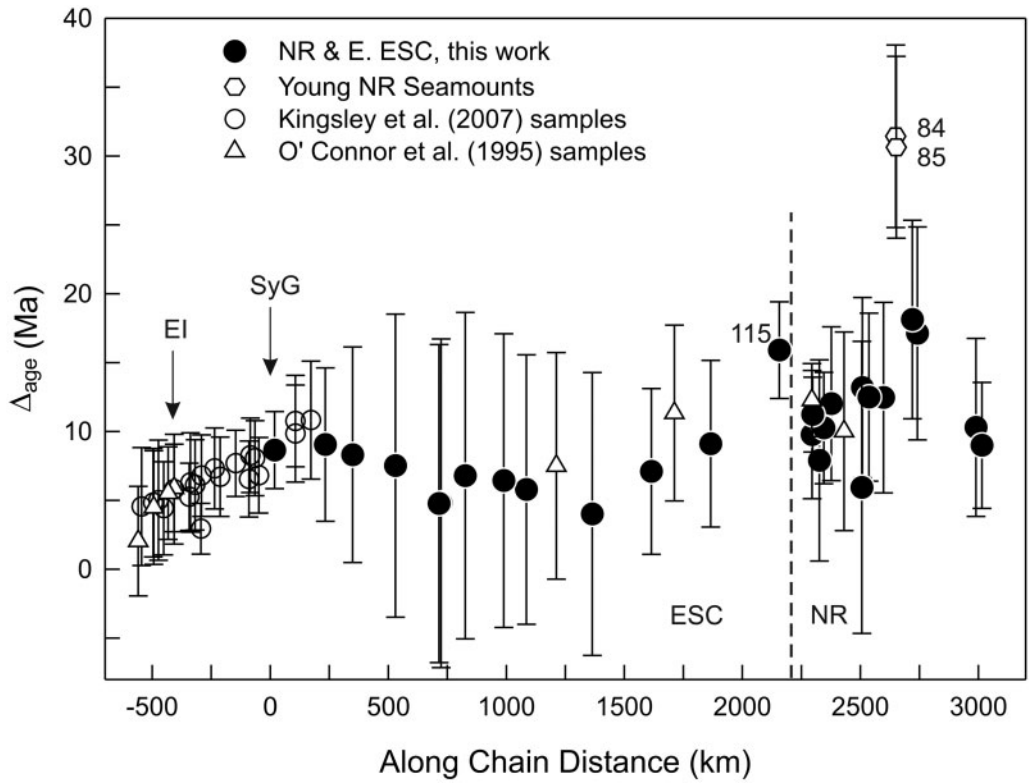


**Fig. 12.** Estimated age of sub-seamount crust at the time of seamount lava eruption ($\Delta_{age}$) vs along-chain distance of the sampling site from SyG. Sample ages used in the $\Delta_{age}$ calculation for Kingsley *et al.*'s (2007) samples from the western ESC are R. A. Duncan's unpublished $^{40}Ar-^{39}Ar$ ages. Other sample ages used are those of O'Connor *et al.* (1995), as indicated. Error bars are 2σ, estimated by propagating errors on the $^{40}Ar-^{39}Ar$ ages of volcanoes and on the seafloor ages from Müller *et al.* (2008). The dashed vertical line roughly marks the boundary between the NR and ESC.

axis, the distance from the spreading axis at the time of volcanism can be estimated. As expected, samples from the ESC west of Salas y Gomez exhibit a westward decrease in $\Delta_{age}$. With the exception of three samples, the western ESC range in $\Delta_{age}$ is fairly narrow, between 4·4 and 9·8 Myr. For our samples from the NR and eastern ESC, $\Delta_{age}$ is <18·1 Myr (excluding the two anomalously young NR samples, for which $\Delta_{age}$ is ~31 Myr). For all but one sample from the ESC east of Salas y Gomez (DRFT 115), $\Delta_{age}$ is between 4·0 and 9·1 Myr, which is very similar to the range observed for the majority of young lavas west of Salas y Gomez. The $\Delta_{age}$ values for the NR samples are higher as a group (5·9–18·1 Myr), but overlap significantly with those for the eastern and western ESC; all but two NR samples have $\Delta_{age}$ between 5·9 and 12·5 Myr (Fig. 12). Thus, the majority of our dated lavas appear to have erupted on seafloor several million years old and therefore well to the east of the EPR (e.g. assuming a spreading half-rate of 10 cma$^{-1}$, a $\Delta_{age}$ of 5 Myr corresponds to a distance of 500 km). The data are too sparse and errors on $\Delta_{age}$ estimates are too high to determine whether there is a pattern of $\Delta_{age}$ with position along the eastern ESC or along or across the NR, but as with other oceanic hotspot volcanoes it is likely that many of the larger seamounts formed over a period of as much as a few million years (O'Connor *et al.*, 1995), so that distance from the axis varied even as a seamount was forming. The ~4 Myr spread in plateau ages of three whole-rock samples from one NR seamount (GS7202-62) and the high $\Delta_{age}$ of 15·9 Myr for the easternmost ESC seamount sampled (DRFT 115) are consistent with such an explanation. The lack of $\Delta_{age}$ values <5·9 Myr among the lavas of the NR could indicate that all of the NR volcanoes formed farther off axis than some of the ESC lavas, but it is also possible that our sampling, which was focused on the flanks of the larger seamounts, simply happened not to retrieve any NR lavas formed closer to the axis.

## Nature of the ESC–NR mantle source

Previous isotopic data for the ESC, nearly all of which are for lavas <2 Ma, have been interpreted as indicating a mantle source composed of a high-$\varepsilon_{Nd}$, relatively low-$^{206}Pb/^{204}Pb$ N-MORB-type component and a lower-$\varepsilon_{Nd}$, high-$^{206}Pb/^{204}Pb$ C/FOZO-like component (Haase *et al.*, 1996; Kingsley & Schilling, 1998; Cheng *et al.*, 1999; Kingsley *et al.*, 2007). Our data for rocks ranging in age from 1·4 to 30 Ma define an array collinear with the previous isotopic array (after the two anomalously young NR lavas and four significantly altered samples are excluded; Fig. 10). Thus, essentially the same two mantle components have dominated volcanism in the ESC–NR system for at least the last 30 Myr. In this respect the Salas–Easter hotspot differs from some other major hotspots (e.g. see Fig. 11), in which more than two components have been expressed at different times and/or places [e.g. Hawaii (e.g. Hanano *et al.*, 2010), Galápagos (e.g. Harpp & White, 2001), Samoa (e.g. Jackson *et al.*, 2010)].

Curve A in Fig. 13a schematically illustrates variable solid-state mixing of two homogeneous source components, a model Pacific N-MORB mantle end-member ($^{206}Pb/^{204}Pb = 17·8$, $\varepsilon_{Nd} = +11·5$) and a broadly C/FOZO-like end-member ($^{206}Pb/^{204}Pb = 20·5$ and $\varepsilon_{Nd} = +2$). Isotopic values used for the N-MORB mantle end-member are among the lowest-$^{206}Pb/^{204}Pb$, highest-$\varepsilon_{Nd}$ compositions observed for the rifts of the Easter Microplate and the southern EPR axis. Those for the C/FOZO-like end-member are estimated from the lowest $\varepsilon_{Nd}$ and highest $^{206}Pb/^{204}Pb$ values in the combined ESC–NR dataset and from companion plots of isotope ratios versus concentration ratios (e.g. Fig. 14a and b). Not surprisingly, these end-member values are very similar to those proposed by earlier workers (see Background). Curve A approximately bisects the available data but significant scatter is present around the curve, indicating that the real end-members are not truly homogeneous and/or that elemental ratios have been modified by melting before or during mixing. Assessing the degree of isotopic and elemental heterogeneity within each mantle end-member is difficult, but assuming homogeneity the range of variation in amount of melting needed to explain the data can be evaluated at least crudely. It can be seen that most of the data are bounded by curves B and C in Fig. 13a. Curve B represents variable mixing of a 7% aggregate fractional melt of the C/FOZO-type end-member and a 0·5% melt of the N-MORB-source end-member, whereas for curve C a 0·5% melt of the C/FOZO-type source mixes with a 7% melt of the N-MORB source. These curves lie within model 'extreme' mixing curves calculated by Kingsley *et al.* (2007) from the maximum and minimum observed Nd/Pb concentration ratios in western ESC lavas, so the actual elemental diversity observed in the lavas is more than sufficient to accommodate mixing equivalent to that of curves B and C.

Figure 13b shows Nd/Pb vs $^{206}Pb/^{204}Pb$. The Nd/Pb ratio is relatively insensitive to fractional crystallization of basaltic magmas but is modified by low-degree partial melting (e.g. Hall *et al.*, 2006). Simple mixing of two homogeneous end-members, whether solids or melts, should lead to lavas that define linear arrays in this diagram (unless Pb concentrations have been modified by post-eruptive alteration). The combined ESC–NR data show no correlation overall, as expected for variable amounts of partial melting superimposed on variable mixing. However, most of the data lie within or rather near the space bounded by lines corresponding to curve A at high Nd/Pb, and curves B and C at low Nd/Pb. Thus, a combination of source mixing and melt mixing with variable partial melting can explain the majority of the data. Several samples have Nd/Pb values significantly outside the envelope bounded

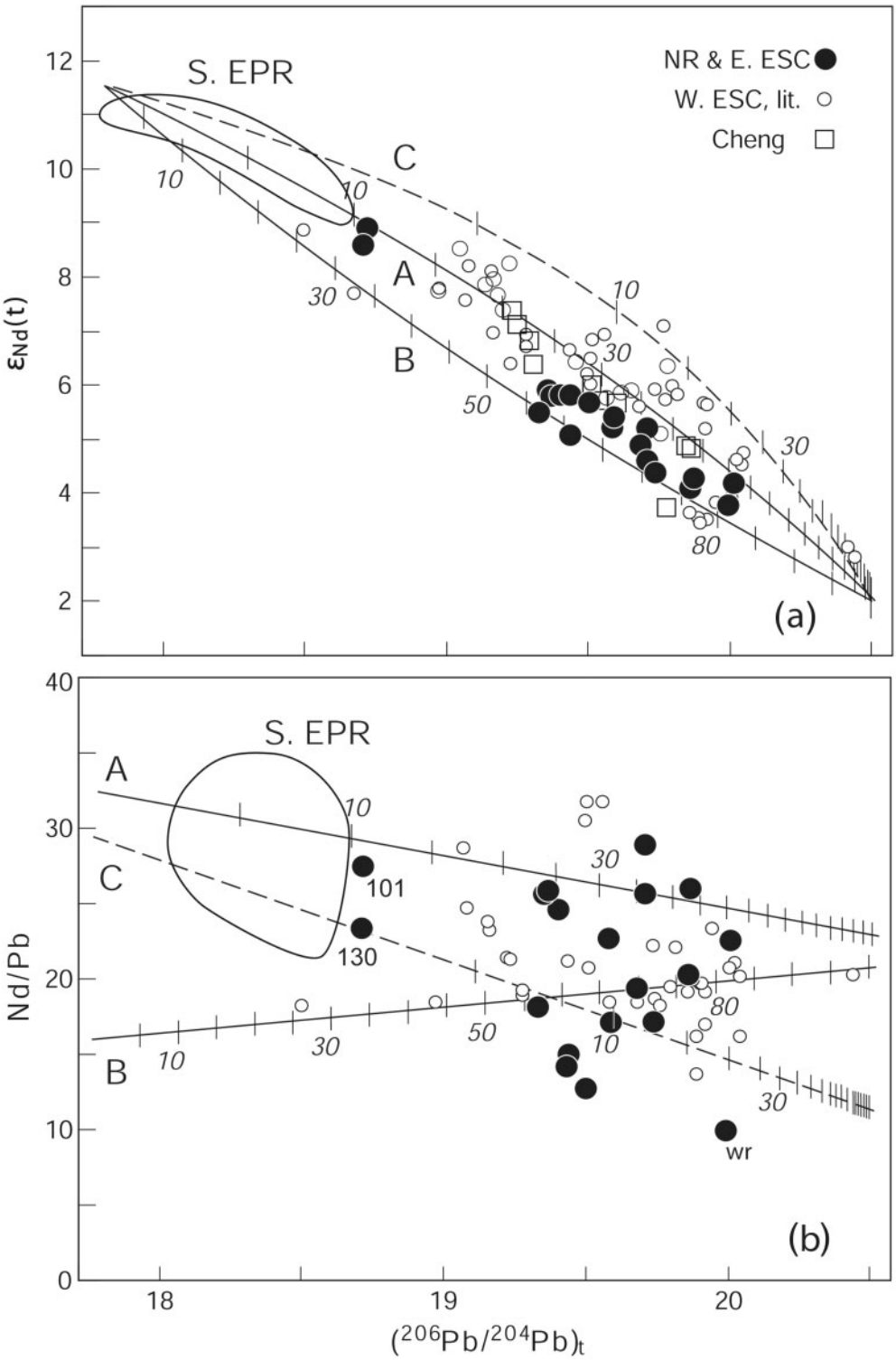


**Fig. 13.** (a) Variation of $\varepsilon_{Nd}(t)$ vs $(^{206}Pb/^{204}Pb)_t$ compared with model binary mixing curves. Data sources are as in Fig. 10. Data for altered samples DRFT 112-1 and 131-1 and the young NR seamount are not shown. Curve A illustrates source mixing of low-$\varepsilon_{Nd}$ C/FOZO-type mantle with N-MORB-source high-$\varepsilon_{Nd}$ mantle, curve B mixing of a 7% aggregate fractional melt of the C/FOZO-type end-member and a 0·5% aggregate fractional melt of the N-MORB-source mantle, and curve C mixing of a 0·5% melt of the C/FOZO-type end-member and a 7% melt of the N-MORB-source end-member. Tick marks represent percentage of the C/FOZO-type end-member in the mixture. (b) Variation of Nd/Pb vs $(^{206}Pb/^{204}Pb)_t$. Points for the two MORB-like samples and the only whole-rock (wr) sample in our dataset are labelled. Lines correspond to the model mixing curves in (a). The equations of Shaw (1970) and bulk partition coefficients of Workman & Hart (2005) were used for calculating the compositions of the aggregate fractional melts. Concentrations of Nd and Pb in the C/FOZO-type end-member are assumed to be 1·73 ppm and 0·076 ppm, and those in the high-$\varepsilon_{Nd}$ end-member to be 0·58 ppm and 0·02 ppm, respectively (Hall *et al.*, 2006). The assumed isotopic compositions of the end-members are $\varepsilon_{Nd} = +2·0$ and $^{206}Pb/^{204}Pb = 20·5$ for the C/FOZO-type end-member, and $\varepsilon_{Nd} = +11·5$ and $^{206}Pb/^{204}Pb = 17·8$ for the high-$\varepsilon_{Nd}$ end-member.

by the model mixing lines. Within the parameters used for constructing the figure, they could represent some combination of intrinsic heterogeneity in one or both source end-members and/or a more complicated melting scenario than modeled.

Interestingly, data for volcanoes east of Salas y Gomez largely lie below curve A in Fig. 13a, as do many of the data for samples from west of Salas y Gomez (including Easter Island). However, data for volcanoes near Salas y Gomez (between about 103·7°W and 108·7°W) are more variable. Isotope ratios for these samples fall both above and below curve A, even at the same $^{206}Pb/^{204}Pb$; for example, a range of 2·5 $\varepsilon_{Nd}$ units is seen at $^{206}Pb/^{204}Pb$ of 19·8–19·9. These samples all have rather high $^{206}Pb/^{204}Pb$ (>19·5), consistent with a relatively large proportion of the C/FOZO-type component (although for a given $^{206}Pb/^{204}Pb$, a point on curve B represents a greater proportion of the C/FOZO-type component than a point on curve C). The reason for this variety near Salas y Gomez is not clear, but we note that it is not an artefact of inter-laboratory analytical bias as most of this subgroup of samples were analyzed in the same laboratory (Kingsley *et al.*, 2007).

In Fig. 10a and b, the positions of data points for the anomalously young NR tephrite and foidite (DRFT 84-1 and 85-1) indicate the presence of San-Felix-type material in the source of these highly alkalic rocks, in addition to C/FOZO-type mantle. The seamount from which these samples were dredged lies ~550 km NNW of the even younger (0·4 Ma; Haase *et al.*, 2000) islands of San Felix and San Ambrosio (Fig. 1). Thus, it seems likely that in the relatively recent past (but before ~5 Ma) the part of the Nazca plate on which this seamount rests overrode a region of asthenosphere containing fertile San-Felix-type mantle. It should be noted that we cannot rule out the possibility that San-Felix-type material is also present in Salas–Easter hotspot mantle and/or below the southern EPR but simply does not show up in the hotspot or ocean ridge lavas because it is a volumetrically minor, early melting component whose signature is swamped once melting of the more prevalent C/FOZO-type and N-MORB-source-type material becomes significant (see Ito & Mahoney, 2005).

## Depth of magma generation

As noted above, the major element relationships in Fig. 6 imply that most NR–ESC magmas were produced by smaller amounts of partial melting at greater mean depths than basalts of the Easter Microplate rifts and southern EPR. Trace elements also can shed some light on the conditions of partial melting. The heavy rare earth elements, in particular, are sensitive indicators of garnet in the source, which in turn provides information on depth of melting. The minimum pressure of garnet stability varies depending on rock composition, but the minimum pressure at

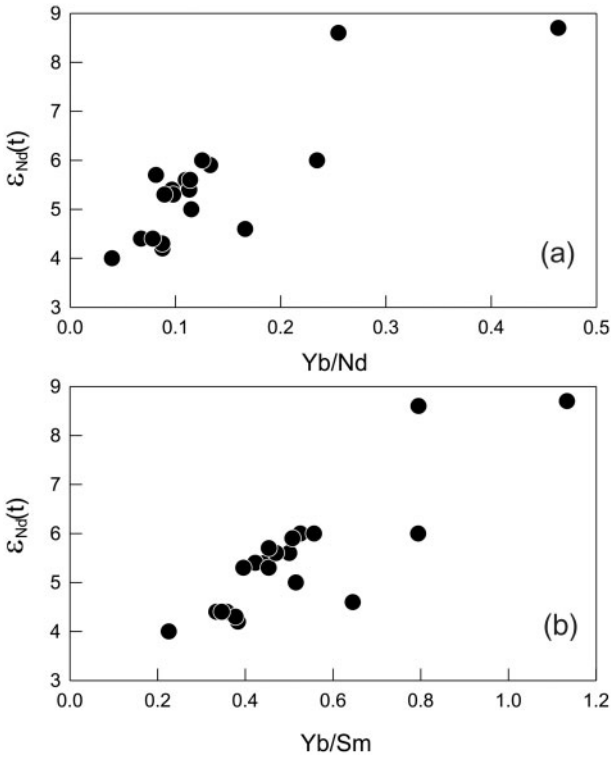


**Fig. 14.** Plots of $\varepsilon_{Nd}(t)$ vs (a) Yb/Nd and (b) Yb/Sm for the data from this study.

which garnet is stable on the anhydrous solidus of fertile peridotite is ~28 kbar, corresponding to a depth of about ~95 km (e.g. Robinson & Wood, 1998). Figure 15 shows chondrite-normalized $(La/Sm)_n$ vs $(Dy/Yb)_n$, with a model grid for melting beginning and ending at different pressures. The REEBOX model (Fram & Lesher, 1993; Fram, 1994; Fram *et al.*, 1998; Tegner *et al.*, 1998) was used to construct the grid, which represents the compositions of pooled melts formed by dynamic non-modal incremental melting. For the calculations summarized in Fig. 15, we assumed a peridotite source and a uniform melt generation rate of 1% per kbar. Because most of our data cluster in a small range of isotopic values [e.g. $\varepsilon_{Nd}(t)$ between +4 and +6], we also assumed, for simplicity, a single source composition corresponding to a 30:70 mixture of incompatible-element-depleted N-MORB-source mantle (DMM) and C/FOZO-type mantle; for the latter, we assumed an estimated primitive mantle (PM) rare earth element composition. The main effect of changing the proportions of the two end-members in the source is to move the grid laterally.

The majority of our ESC–NR data and of the western ESC data from the literature fall well within the grid. The implication is that most ESC–NR lavas represent relatively small mean amounts of partial melting (generally less than about 7% in the model summarized in the

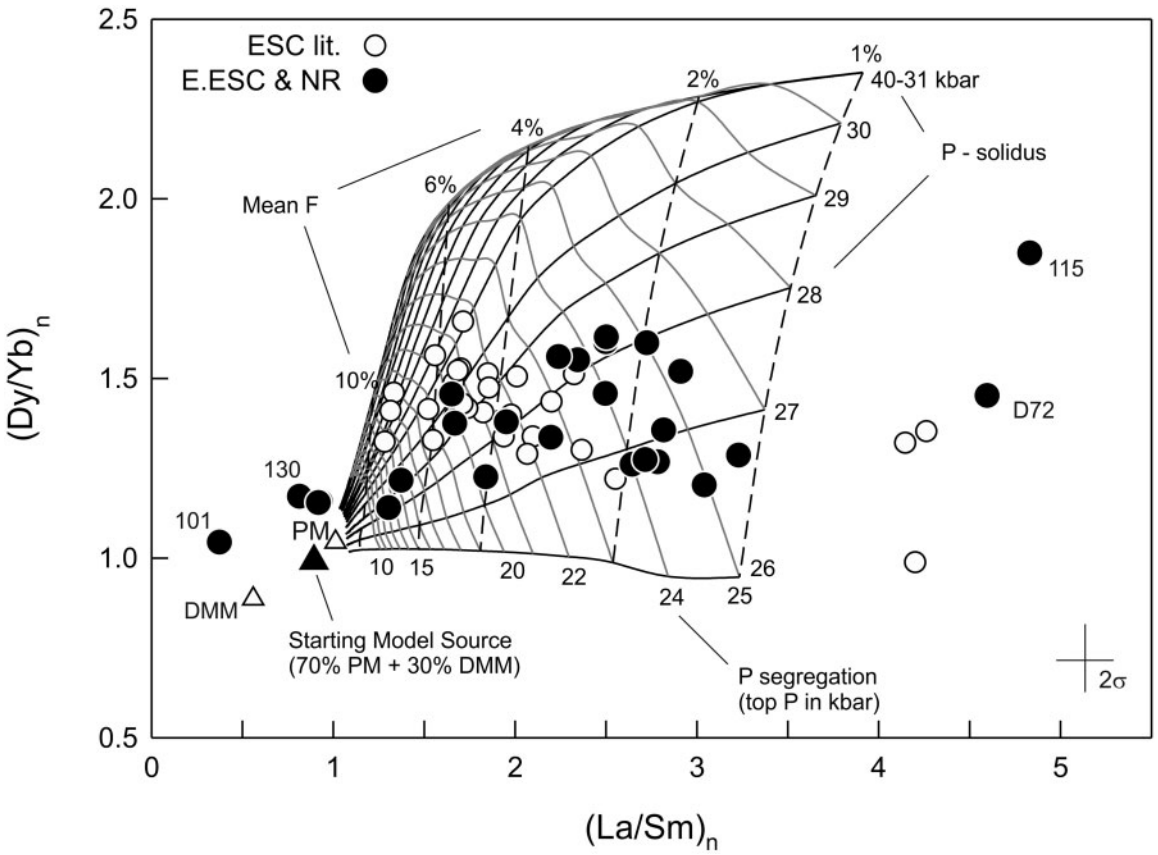


**Fig. 15.** Chondrite-normalized $(La/Sm)_n$ vs $(Dy/Yb)_n$ for the data from this study (E. ESC & NR; excluding DRFT 84-1 and 85-1) and data from the literature (ESC lit., sources as in Fig. 8). Curves are for pooled melts generated by polybaric, non-modal, incremental melting of peridotite using the REEBOX model (Fram & Lesher, 1993; Fram *et al.*, 1998; Tegner *et al.*, 1998). Bold continuous black contours depict evolutionary paths of pooled melts for melting beginning at various pressures (i.e. *P*-solidus = 40–26 kbar) and terminating at 0 kbar. Contours of pressure at the top of the melting zone (*P*-segregation) are shown in light gray. Dashed curves are contours of mean *F* (fraction of melting). The model unmelted source is a mixture of 70% of C/FOZO-type mantle [assumed to be equivalent to estimated primitive mantle or PM (Lyubetskaya & Korenaga, 2007) for these elements] and 30% of depleted N-MORB-source mantle [estimate of Salters & Stracke (2004)]; initial mineral proportions of olivine:orthopyroxene:clinopyroxene:garnet:spinel:plagioclase are 0·55:0·15:0·20:0·10:0·0:0·0. Mineral–melt partition coefficients are from Green (1994) and melting reactions are from Elliott *et al.* (1991), Kinzler & Grove (1992) and Fram (1994). Reaction coefficients are assumed to be linear between 30 and 20 kbar for the garnet–spinel transition, and between 14 and 10 kbar for the spinel–plagioclase transition. Open triangles represent the pure C/FOZO (PM) mantle and DMM end-members. The 2σ errors on the elemental ratios are determined from analytical uncertainties.

figure) that began in the garnet stability zone. Also, a rather wide range of melt segregation pressures throughout the spinel peridotite stability zone is indicated. In contrast, data for five of our samples lie outside the model grid in Fig. 15. The three with $(La/Sm)_n < 1$ are the N-MORB-like tholeiites from dredges DRFT 101 and 130. Increasing the proportion of DMM in the model source moves the grid leftward enough to include the two DRFT 130 samples, but DRFT 101-2 has even lower $(La/Sm)_n$ (0·39) than any published estimate of global DMM of which we are aware. Because the isotope ratios of this basalt, although N-MORB-like [e.g. $\varepsilon_{Nd}(t) = +8{\cdot}7$], are not near the high-$\varepsilon_{Nd}$, low-$^{87}Sr/^{86}Sr$, low-$^{206}Pb/^{204}Pb$ end of the Pacific MORB spectrum, we infer that the source of this sample may have experienced previous, relatively recent removal of a small melt fraction. Two of our highly alkalic samples, phonotephrite DRFT 115-1 and basaltic trachyandesite GS7202-72-2 [and three highly alkalic basaltic trachyandesite samples analyzed by Puzankov & Bobrov (1997)] have very high $(La/Sm)_n$ values (>4), placing them well to the right of the model grid. These compositions cannot be explained by increasing the proportion of the C/FOZO-type end-member in the model source, even to 100%. The isotopic ratios of these samples are not at the low-$\varepsilon_{Nd}$, low-$^{87}Sr/^{86}Sr$, low-$^{206}Pb/^{204}Pb$ end of the ESC–NR array, and their data points lie well off to the high-$(La/Sm)_n$ side of the trend formed by the other samples in, for example, an $\varepsilon_{Nd}(t)$ vs $(La/Sm)_n$ diagram (not shown). We speculate that such compositions may indicate re-melting of small melt fractions that did not escape the melting zone.

Overall, the results are consistent with formation of the majority of lavas well off axis, in agreement with the 5–13

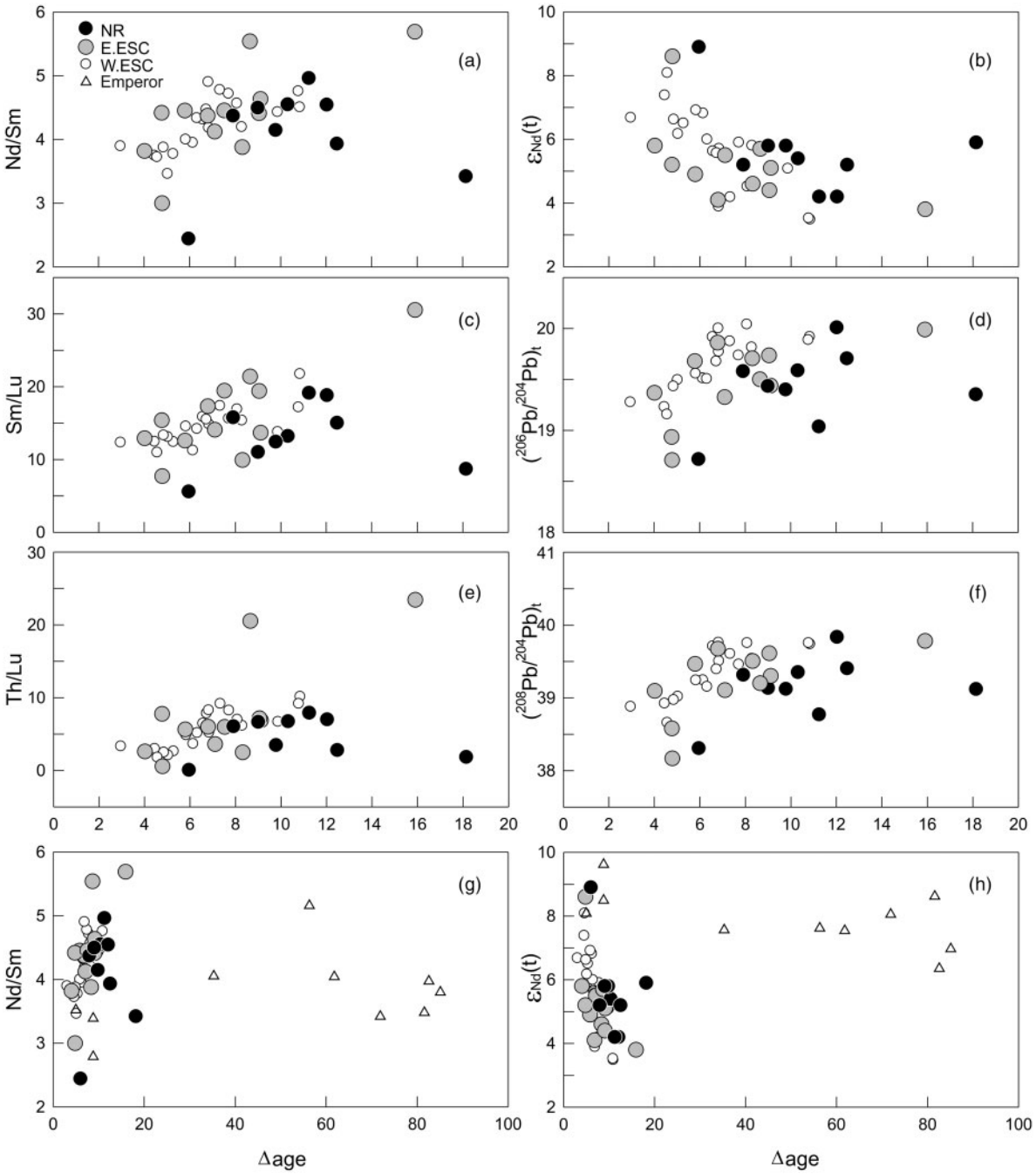


**Fig. 16.** Variation of isotopic and incompatible element ratios with $\Delta_{age}$ for the NR, eastern (E.) ESC, and western (W.) ESC (a–f). In (g) and (h), data for the Emperor Seamounts are included (note the change in the $\Delta_{age}$ scale). Data for the young NR seamount (DRFT 84-1 and 85-1) are far off scale to the right in (a–f) and are not shown in (g) or (h). Sources for the ESC and NR data: Kingsley *et al.* (2002, 2007) and this work. Source for the Emperor Seamount geochemical data: Regelous *et al.* (2003); $\Delta_{age}$ values for the Emperor Seamounts are from Caplan-Auerbach *et al.* (2000).

Myr $\Delta_{age}$ values of most samples. Lithospheric thickness generally increases with increasing seafloor age (e.g. Stein & Stein, 1993); thus, the $\Delta_{age}$ value is broadly related to the thickness of the lithosphere at the time of seamount volcanism, which in turn provides a rough upper (shallow) limit on the depth of melt segregation (i.e. the top of the melting zone). Despite the large uncertainties in $\Delta_{age}$ and except for a few outliers, the incompatible-element and isotopic data for most samples from the ESC–NR show crude correlations with $\Delta_{age}$ (Fig. 16) that are qualitatively

consistent with greater mean depths of partial melting and an increased expression of the C/FOZO-type component at higher $\Delta_{age}$, which could be a result of a greater contribution from this enriched component at lower degrees of melting beneath thicker lithosphere. Interestingly, data for the Emperor Seamounts (Regelous *et al.*, 2003) show somewhat similar relationships with $\Delta_{age}$, but the range in isotopic and incompatible element ratios is smaller and the range in $\Delta_{age}$ is much greater, from less than 10 Myr to more than 80 Myr (Fig. 6g and h).

## CONCLUSIONS

Volcanoes of the ESC and NR exhibit an age vs distance relationship that demonstrates that the two features are part of the same, >30 Ma, hotspot trail and is consistent with a hotspot center near Salas y Gomez Island. The relative position of the hotspot to the Pacific–Nazca spreading axis appears to have varied over a rather limited range during construction of the eastern ESC seamounts (i.e. east of Salas y Gomez) and, in general, the NR, judging from the observation that most dated lavas were erupted onto seafloor that was between 5 and 13 Myr old. The same is also true for the ESC west of Salas y Gomez, but several of these lavas appear to have been emplaced onto younger seafloor and thus probably closer to the spreading axis. Construction of the NR terminated, and that of the ESC began, at about 23 Ma. This change marks a change in the direction of Nazca plate motion that very probably is related to Farallon plate breakup (Barckhausen *et al.*, 2008) and coincides approximately with a change in Pacific plate motion (Wessel & Kroenke, 2000).

Most lavas sampled east of Salas y Gomez are moderately alkalic to transitional basalts. They appear to represent fairly small mean amounts of partial melting beginning in garnet-bearing mantle and ending in the spinel facies. Isotopic compositions are within the range previously determined for the western ESC volcanoes, and indicate that the mantle source has consisted of the same two principal components since at least 30 Ma. In agreement with the conclusions of studies of the western ESC (e.g. Haase *et al.*, 1996; Cheng *et al.*, 1999; Kingsley *et al.*, 2007), these are a C/FOZO-type component and a high-$\varepsilon_{Nd}$, incompatible-element-depleted Pacific MORB-source-type component. However, most of our data cluster in a relatively small isotopic range [e.g. $\varepsilon_{Nd}(t)$ +4 to +6] closer to the inferred C/FOZO-type composition. This result suggests limited variation in the proportions of each component in the mantle source and/or that the conditions of melting and melt mixing tended to vary within a relatively limited range. The latter interpretation is consistent with the rather small spread of seafloor ages at the time of volcanism (i.e. distance of a seamount from the spreading axis) for most of our samples. However, we note that in the western ESC the high-$\varepsilon_{Nd}$, more N-MORB-like basalts are found mainly on low-lying volcanic features (e.g. Haase & Devey, 1996). It is possible that similar lavas are also present along the eastern ESC and NR, but that few were recovered simply because we concentrated our dredging on the upper flanks of the larger seamounts.

## ACKNOWLEDGEMENTS

We are grateful to the crew of the R.V. *Roger Revelle* and marine technicians of the Scripps Institution of Oceanography for making Leg 6 of the Drift expedition a success. We thank Doug Pyle, Kevin Johnson and Hetu Sheth for their help during dredging and sub-sampling, and Kent Ross and Denys Vonderhaar for providing support during chemical analyses of samples at the University of Hawaii. We thank Debra Stakes for samples from cruise 14 of the R.V. *Dmitry Mendeleev*, Jim Natland for GS7202 samples from the dredged rock collection at the University of Miami, and Charles Lesher for the REEBOX program. The paper greatly benefited from critical reviews by C. Class, M. Regelous and J. M. O'Connor.

## FUNDING

This work was funded by NSF grants OCE0002875 (R.D.) and OCE0004498 (J.M.).

## REFERENCES

Albarède, F. (2001). Radiogenic ingrowth in systems with multiple reservoirs: applications to the differentiation of the mantle–crust system. *Earth and Planetary Science Letters* **188**, 59–73.

Bach, W., Hegner, E., Erzinger, J. & Satir, M. (1994). Chemical and Isotopic variations along the superfast spreading East Pacific Rise from 6° to 30°S. *Contributions to Mineralogy and Petrology* **116**, 365–380.

Barckhausen, U., Ranero, C. R., Cande, S. C., Engels, M. & Weinrebe, W. (2008). Birth of an intraoceanic spreading center. *Geology* **36**, 767–770.

Beier, C., Vanderkluysen, L., Regelous, M., Mahoney, J. J. & Garbe-Schönberg, D. (2011). Lithospheric control on geochemical composition along the Louisville Seamount Chain. *Geochemistry, Geophysics, Geosystems*, **12**, Q0AM01, doi:10.1029/2011GC003690, 2011..

Bonatti, E., Harrison, C. G. A., Fisher, D. E., Honnorez, J., Schilling, J.-G., Stipp, J. J. & Zentilli, M. (1977). Easter volcanic chain (southeast Pacific): a mantle hot line. *Journal of Geophysical Research* **82**, 2457–2478.

Caplan-Auerbach, J., Duennebier, F. & Ito, G. (2000). Origin of intraplate volcanoes from guyot heights and oceanic paleodepth. *Journal of Geophysical Research* **105**, 2679–2697.

Cheng, Q. C., Macdougall, J. D. & Zhu, P. (1999). Isotopic constraints on the Easter Seamount Chain source. *Contributions to Mineralogy and Petrology* **135**, 225–233.

Clark, J. G. & Dymond, J. (1977). Geochronology and petrochemistry of Easter and Sala y Gomez islands: implications for the origin of the Sala y Gomez ridge. *Journal of Volcanology and Geothermal Research* **2**, 29–48.

Courtillot, V., Davaille, A., Besse, J. & Stock, J. (2003). Three distinct types of hotspots in the Earth's mantle. *Earth and Planetary Science Letters* **205**, 295–308.

Dosso, L., Bougault, H., Langmuir, C., Bollinger, C., Bonnier, O. & Etoubleau, J. (1999). The age and distribution of mantle heterogeneity along the Mid-Atlantic Ridge (31–41°N). *Earth and Planetary Science Letters* **170**, 269–286.

Eakins, B. W. & Lonsdale, P. F. (2005). Structural patterns and tectonic history of the Bauer microplate, Eastern Tropical Pacific. *Marine Geophysical Researches* **24**, 171–205.

Eggins, S. M., Woodhead, J. D., Kinsley, L. P. J., Mortimer, G. E., Sylvester, P., McCulloch, M. T., Hergt, J. M. & Handler, M. R. (1997). A simple method for the precise determination of ≥40 trace elements in geological samples by ICPMS using enriched isotope internal standardisation. *Chemical Geology* **134**, 311–326.

Elliott, T. R., Hawkesworth, C. J. & Grönvold, K. (1991). Dynamic melting of the Iceland plume. *Nature* **351**, 201–206.

Espurt, N., Baby, P., Brusset, S., Roddaz, M., Hermoza, W., Regard, V., Antoine, P. O., Salas-Gismondi, R. & Bolanos, R. (2007). How does the Nazca Ridge subduction influence the modern Amazonian foreland basin? *Geology* **35**, 515–518.

Expedition 330 Scientists. (2011). Louisville Seamount Trail: implications for geodynamic mantle flow models and the geochemical evolution of primary hotspots. *IODP Preliminary Report* **330**, doi:10.2204/iodp.pr.330.2011.

Fitton, J. G. (2007). The OIB paradox. In: Foulger, G. R. & Jurdy, D. M. (eds.), *Plates, Plumes, and Planetary Processes. Geological Society of America, Special Papers* **430**, 387–412.

Fontignie, D. & Schilling, J. G. (1991). $^{87}Sr/^{86}Sr$ and REE variations along the Easter Microplate boundaries (South Pacific): application of multivariate statistical analyses to ridge segmentation. *Chemical Geology* **89**, 209–241.

Fram, M. S. (1994). Petrogenesis of the Early Tertiary flood basalts of the East Greenland continental margin, PhD dissertation, Columbia University, New York, 255 pp.

Fram, M. S. & Lesher, C. E. (1993). Geochemical constraints on mantle melting during creation of the North Atlantic basin. *Nature* **363**, 712–715.

Fram, M. S., Lesher, C. E. & Volpe, A. M. (1998). Mantle melting systematics: Transition from continental to oceanic volcanism on the southeast Greenland margin. In: Saunders, A. D., Larsen, H. C. & Wise, S. W., Jr (eds) *Proceedings of the Ocean Drilling Program, Scientific Results, 152*, College Station, TX: Ocean Drilling Program **152**373–386.

Fretzdorff, S., Haase, K. M. & Garbe-Schönberg, C. D. (1996). Petrogenesis of lavas from the Umu Volcanic Field in the young hotspot region west of Easter Island, southeastern Pacific. *Lithos* **38**, 23–40.

Galer, S. J. G. (1999). Optimal double and triple spiking for high precision lead isotopic measurement. *Chemical Geology* **157**, 255–274.

Gerlach, D. C., Hart, S. R., Morales, V. W. J. & Palacios, C. (1986). Mantle heterogeneity beneath the Nazca plate: San Felix and Juan Fernandez islands. *Nature* **322**, 165–169.

Govindaraju, K. (1994). Compilation of working values and sample description for 383 geostandards. *Geostandards Newsletter* **18**, 1–158.

Green, T. H. (1994). Experimental studies of trace element partitioning applicable to igneous petrogenesis—Sedona 16 years later. *Chemical Geology* **117**, 1–36.

Haase, K. M. (2002). Geochemical constraints on magma sources and mixing processes in Easter Microplate MORB (SE Pacific): a case study of plume–ridge interaction. *Chemical Geology* **182**, 335–355.

Haase, K. M. & Devey, C. W. (1996). Geochemistry of lavas from the Ahu and Tupa volcanic fields, Easter Hotspot, SE Pacific: implications for intraplate magma genesis near a spreading axis. *Earth and Planetary Science Letters* **137**, 129–143.

Haase, K. M., Devey, C. W. & Goldstein, S. L. (1996). Two-way exchange between the Easter mantle plume and the Easter microplate spreading axis. *Nature* **382**, 344–346.

Haase, K. M., Stoffers, P. & Garbe-Schönberg, C.-D. (1997). The petrogenetic evolution of lavas from Easter Island and neighbouring seamounts, near-ridge hotspot volcanoes in the SE Pacific. *Journal of Petrology* **38**, 785–813.

Haase, K. M., Mertz, D. F., Sharp, W. S. & Garbe-Schönberg, C.-D. (2000). Sr–Nd–Pb isotopic ratios, geochemical compositions, and $^{40}Ar/^{39}Ar$ data of lavas from San Felix Island (Southeast Pacific): Implications for magma genesis and sources. *Terra Nova* **12**, 90–96.

Hall, L. S. & Sinton, J. M. (1996). Geochemical diversity of the large lava field on the flank of the East Pacific Rise at 8°17'S. *Earth and Planetary Science Letters* **142**, 241–251.

Hall, L. S., Mahoney, J. J. & Sinton, J. M. (2006). Spatial and temporal distribution of a C-like asthenospheric component in the Rano Rahi Seamount Field, East Pacific Rise, 15°–19°S. *Geochemistry, Geophysics, Geosystems* **7**, Q03009, doi:10.1029/2005GC000994.

Hanan, B. B. & Graham, D. W. (1996). Lead and helium isotope evidence from oceanic basalts for a common deep source of mantle plumes. *Science* **272**, 991–995.

Hanan, B. B. & Schilling, J.-G. (1989). Easter microplate evolution: Pb isotope evidence. *Journal of Geophysical Research* **94**, 7432–7448.

Hanano, D., Weis, D., Scoates, J. S., Aciego, S. & DePaolo, D. J. (2010). Horizontal and vertical zoning of heterogeneities in the Hawaiian mantle plume from the geochemistry of consecutive postshield volcano pairs: Kohala–Mahukona and Mauna Kea–Hualalai. *Geochemistry, Geophysics, Geosystems* **11**, Q01004, doi:10.1029/2009GC002782.

Harada, Y., Wessel, P., Naar, D. F., Wilder, D. T., Duncan, R. A., Mahoney, J. J., Johnson, K. T. M., Pyle, D. G. & Ray, J. S. (2003). Nazca absolute plate motion and Pacific basin inter-hotspot motion. In: *Proceedings of the EGS–AGU–EUG Joint Assembly Nice, France*, O-0010, 48.

Harpp, K. S. & White, W. M. (2001). Tracing a mantle plume; isotopic and trace element variations of Galápagos seamounts. *Geochemistry, Geophysics, Geosystems* **2**, 1042, doi:10.1029/2000GC000137.

Hékinian, R., Bideau, D., Cannat, M., Francheteau, J. & Hebert, R. (1992). Volcanic activity and crust–mantle exposure in the ultrafast Garrett transform fault near 13°28'S in the Pacific. *Earth and Planetary Science Letters* **108**, 259–275.

Hékinian, R., Stoffers, P., Akermand, D., Binard, N., Francheteau, J., Devey, C. & Garbe-Schönberg, D. (1995). Magmatic evolution of the Easter microplate–Crough seamount region (South East Pacific). *Marine Geophysical Researches* **17**, 375–397.

Ingle, S., Mahoney, J. J., Sato, H., Kimura, J. I., Hirano, N., Coffin, M. F. & Nakanishi, M. (2007). Depleted mantle wedge and sediment fingerprint in basalts from the Manihiki Plateau, Central Pacific Ocean. *Geology* **35**, 595–598, doi:10.1130/G23741A.1.

Ito, G. & Mahoney, J. J. (2005). Flow and melting of a heterogeneous mantle: 1. Method and importance to the geochemistry of ocean island and mid-ocean ridge basalts. *Earth and Planetary Science Letters* **230**, 29–46.

Jackson, M. G., Hart, S. R., Konter, J. G., Koppers, A. A. P., Staudigel, H., Kurz, M. D., Blusztajn, J. & Sinton, J. M. (2010). Samoan hot spot track on a 'hot spot highway': Implications for mantle plumes and a deep Samoan mantle source. *Geochemistry, Geophysics, Geosystems* **11**, doi:10.1029/2010GC003232.

Kingsley, R. H. & Schilling, J.-G. (1998). Plume–ridge interaction in the Easter–Salas y Gomez seamount chain–Easter Microplate system: Pb isotope evidence. *Journal of Geophysical Research* **103**, 24159–24177.

Kingsley, R. H., Schilling, J.-G., Dixon, J. E., Swart, P., Poreda, R. & Simons, K. (2002). D/H ratios in basalt glasses from the Salas y Gomez mantle plume interacting with the East Pacific Rise: water from old D-rich recycled crust or primordial water from the lower mantle? *Geochemistry, Geophysics, Geosystems* **3**, doi:10.1029/2001GC000199.

Kingsley, R. H., Blichert-Toft, J., Fontignie, D. & Schilling, J.-G. (2007). Hafnium, neodymium, and strontium isotope and parent–daughter element systematics in basalts from the plume–ridge interaction system of the Salas y Gomez Seamount Chain and Easter Microplate. *Geochemistry, Geophysics, Geosystems* **8**, doi:10.1029/2006GC001401.

Kinzler, R. J. & Grove, T. L. (1992). Primary magmas of mid-ocean ridge basalts, 1. Experimental methods. *Journal of Geophysical Research* **97**, 6885–6906.

Klein, E. M. & Langmuir, C. H. (1987). Global correlations of ocean ridge basalt chemistry with axial depth and crustal thickness. *Journal of Geophysical Research* **92**, 8089–8115.

Koppers, A. A. P. (2002). ArArCALC—software for Ar-40/Ar-39 age calculations. *Computers and Geosciences* **28**, 605–619.

Koppers, A. A. P., Staudigel, H. & Duncan, R. A. (2003). High-resolution $^{40}Ar/^{39}Ar$ dating of the oldest oceanic basement basalts in the western Pacific basin. *Geochemistry, Geophysics, Geosystems* **4**, doi:10.1029/2003GC000574.

Koppers, A. A. P., Duncan, R. A. & Steinberger, B. (2004). Implications of a nonlinear $^{40}Ar/^{39}Ar$ age progression along the Louisville seamount trail for models of fixed and moving hot spots. *Geochemistry, Geophysics, Geosystems* **5**, Q06L02, doi:10.1029/2003GC000671.

Kruse, S. E., Liu, Z. J. & Naar, D. F. (1997). Effective elastic thickness of the lithosphere along the Easter Seamount Chain. *Journal of Geophysical Research* **102**, 27305–27317.

Kullerud, L. (1991). On the calculation of isochrons. *Chemical Geology* **87**, 115–124.

Le Maitre, R. W. (1989). *A Classification of Igneous Rocks and Glossary of Terms: Recommendations of the International Union of Geological Sciences Subcommission on the Systematics of Igneous Rocks*. Oxford: Blackwell, 193 p.

Liu, Z. (1996). The origin and evolution of the Easter seamount chain, PhD thesis, University of South Florida, St. Petersburg, 266 pp.

Lyubetskaya, T. & Korenaga, J. (2007). Chemical composition of Earth's primitive mantle and its variance: 2. Implications for global geodynamics. *Journal of Geophysical Research* **112**, B03212, doi:10.1029/2005JB004224.

Macdonald, G. A. & Katsura, T. (1964). Chemical composition of Hawaiian lavas. *Journal of Petrology* **5**, 82–133.

Macdougall, J. D. & Lugmair, G. W. (1986). Sr and Nd isotopes in basalts from the East Pacific Rise: significance for mantle heterogeneity. *Earth and Planetary Science Letters* **77**, 273–284.

Mahoney, J. J. (1987). An isotopic survey of Pacific oceanic plateaus: implications for their nature and origin. In: Keating, B. H., Fryer, P., Batiza, R. & Boehlert, G. (eds). *Seamounts, Islands and Atolls. American Geophysical Union, Geophysical Monograph* **43**, 207–220.

Mahoney, J. J., Sinton, J. M., Kurz, M. D., Macdougall, J. D., Spencer, K. J. & Lugmair, G. W. (1994). Isotope and trace element characteristics of a superfast spreading ridge: East Pacific Rise, 13–23°S. *Earth and Planetary Science Letters* **121**, 173–193.

Mahoney, J. J., Graham, D. W., Christie, D. M., Johnson, K. T. M., Hall, L. S. & Vonderhaar, D. L. (2002). Between a hotspot and a cold spot: isotopic variation in the Southeast Indian Ridge asthenosphere, 86°E–118°E. *Journal of Petrology* **43**, 1155–1176.

Mahoney, J. J., Duncan, R. A., Tejada, M. L. G., Sager, W. W. & Bralower, T. J. (2005). A Jurassic–Cretaceous boundary age and MORB-type mantle source for Shatsky Rise. *Geology* **33**, 185–188.

Mammerickx, J. (1981). Depth anomalies in the Pacific: Active, fossil and precursor. *Earth and Planetary Science Letters* **53**, 147–157.

Mammerickx, J. & Sandwell, D. (1986). Rifting of old oceanic lithosphere. *Journal of Geophysical Research* **91**, 1975–1988.

Mayes, C. L., Lawver, L. A. & Sandwell, D. T. (1990). Tectonic history and new isochron chart of the South Pacific. *Journal of Geophysical Research* **95**, 8543–8567.

Montelli, R., Nolet, G., Dahlen, F. A. & Masters, G. (2006). A catalogue of deep mantle plumes: new results from finite-frequency tomography. *Geochemistry, Geophysics, Geosystems* **7**, Q11007, doi:10.1029/2006GC001248.

Morgan, W. (1972). Plate motions and deep mantle convection. In: Shagam, R., Hargraves, R. B., Morgan, W. J., Van Houten, F. B., Burk, C. A., Holland, H. D. & Hollister, L. C. (eds) *Studies in Earth and Space Sciences: A Memoir in Honor of Harry Hammond Hess, Geological Society of America, Memoirs* **132**, 7–22.

Müller, R. D., Sdrolias, M., Gaina, C. & Roest, W. R. (2008). Age, spreading rates and spreading symmetry of the world's ocean crust. *Geochemistry, Geophysics, Geosystems* **9**, Q04006, doi:10.1029/2007GC001743.

Naar, D. F. & Hey, R. N. (1991). Tectonic evolution of the Easter microplate. *Journal of Geophysical Research* **96**, 7961–7993.

Naar, D. F. & Wessel, P. (2000). Hotspotting the Easter–Salas y Gomez-Nazca Seamount Chain. *EOS Transactions, American Geophysical Union* **81**, F1374.

Naar, D. F., Liu, Z. J., Rappaport, Y., Batiza, R., Hagen, R., Hey, R. N., Nelson, R., Plake, T., Stefani, R., Schilling, J.-G., Kincaid, C., Xu, G., Poreda, R., Joseph, L., Jacobs, C., Beale, V., Bishop, V., Harris, A., Rusby, R., Fontignie, D., Woods, A., Kruse, S., Korenaga, J., Seama, N., Vergara, H. & Guarda, R. (1993). GLORI-B and geochemical investigation of the Easter Seamount Chain to San Ambrosia Island. *EOS Transactions, American Geophysical Union* **74**, F672.

Naar, D. F., Johnson, K. T. M., Wessel, P. & Pyle, D. G. (2002). Preliminary mapping and dredging results along the Nazca Ridge and Easter/Salas y Gomez Chain. *EOS Transactions, American Geophysical Union* **83(4)**, OS273.

Neal, C. R. (2001). The interior of the Moon: the presence of garnet in the primitive, deep lunar mantle. *Journal of Geophysical Research* **106**, 27865–27885.

Niu, Y. & Hékinian, R. (1997). Basaltic liquids and harzburgitic residues in the Garrett Transform: A case study at fast-spreading ridges. *Earth and Planetary Science Letters* **146**, 243–258.

O'Connor, J. M., Stoffers, P. & McWilliams, M. O. (1995). Time–space mapping of Easter Chain volcanism. *Earth and Planetary Science Letters* **136**, 197–212.

Okal, E. A. & Cazenave, A. (1985). A model for the plate tectonic evolution of the east–central Pacific based on Seasat investigations. *Earth and Planetary Science Letters* **72**, 99–116.

Pan, Y. & Batiza, R. (1998). Major element chemistry of volcanic glasses from the Easter Seamount Chain: constraints on melting conditions in the plume. *Journal of Geophysical Research* **103**, 5287–5304.

Puzankov, Yu. M. & Bobrov, V. A. (1997). Geochemistry of the volcanic rocks from Easter and Sala y Gomez islands. *Geochemistry International* **35**, 609–619.

Regelous, M., Hofmann, A. W., Abouchami, W. & Galer, S. J. G. (2003). Geochemistry of lavas from the Emperor Seamounts, and the geochemical evolution of Hawaiian magmatism from 85 to 42 Ma. *Journal of Petrology* **44**, 113–140.

Renne, P. R., Swisher, C. C., Deino, A. L., Karner, D. B., Owens, T. L. & DePaolo, D. J. (1998). Intercalibration of standards, absolute ages and uncertainties in $^{40}Ar/^{39}Ar$ dating. *Chemical Geology* **145**, 117–152.

Robinson, J. A. C. & Wood, B. J. (1998). The depth of the spinel to garnet transition at the peridotite solidus. *Earth and Planetary Science Letters* **164**, 277–284.

Salters, V. J. M. & Stracke, A. (2004). Composition of the depleted mantle. *Geochemistry, Geophysics, Geosystems* **5**, Q05004, doi:05010.01029/02003GC000597.

Schiano, P., Birck, J.-L. & Allègre, C. J. (1997). Osmium–strontium–neodymium–lead isotopic covariations in mid-ocean ridge basalt glasses and the heterogeneity of the upper mantle. *Earth and Planetary Science Letters* **150**, 363–379.

Shaw, D. M. (1970). Trace element fractionation during anatexis. *Geochimica et Cosmochimica Acta* **34**, 237–243.

Simons, K., Dixon, J., Schilling, J.-G., Kingsley, R. & Poreda, R. (2002). Volatiles in basaltic glasses from the Easter–Salas y Gomez Seamount Chain and Easter Microplate: Implications for geochemical cycling of volatile elements. *Geochemistry, Geophysics, Geosystems* **3**, doi:10.1029/2001GC000173.

Sinton, J. M., Smaglik, S. M., Mahoney, J. J. & Macdonald, K. C. (1991). Magmatic processes at superfast spreading mid-ocean ridges: Glass compositional variations along the East Pacific Rise 13°–23°S. *Journal of Geophysical Research* **96**, 6133–6155.

Smith, W. H. F. & Sandwell, D. T. (1997). Global sea floor topography from satellite altimetry and ship depth soundings. *Science* **277**, 1956–1962.

Steiger, R. H. & Jäger, E. (1977). Subcommission on geochronology: convention on the use of decay constants in geo- and cosmochronology. *Earth and Planetary Science Letters* **36**, 359–362.

Stein, C. A. & Stein, S. (1993). Constraints on Pacific midplate swells from global depth-age and heat flow-age models. In: Pringle, M., Sager, W., Sliter, W. & Stein, S. (eds) *The Mesozoic Pacific: Geology, Tectonics, and Volcanism. American Geophysical Union, Geophysical Monograph* **77**, 53–76.

Steinberger, B. (2002). Motion of the Easter hot spot relative to Hawaii and Louisville hot spots. *Geochemistry, Geophysics, Geosystems* **3**, 8503, doi:10.1029/2002GC000334.

Steinberger, B. & O'Connell, R. J. (1998). Advection of plumes in mantle flow; implications on hotspot motion, mantle viscosity and plume distribution. *Geophysical Journal International* **132**, 412–434.

Stracke, A., Hofmann, A. W. & Hart, S. R. (2005). FOZO, HIMU, and the rest of the mantle zoo. *Geochemistry, Geophysics, Geosystems* **6**, Q05007, doi:10.1029/2004GC000824.

Sun, S.-S. & McDonough, W.F. (1989). Chemical and isotopic systematics of oceanic basalts: Implications for mantle composition and processes. In: Saunders, A. D. & Norry, M. J. (eds) *Magmatism in the Ocean Basins. Geological Society*, London: Special Publications **42**313–345.

Taylor, J. R. (1997). *An Introduction to Error Analysis: The Study of Uncertainties in Physical Measurements*. Mill Valley, CA: University Science Books, 327 p.

Tegner, C., Lesher, C. E., Larsen, H. C. & Watt, W. S. (1998). Evidence from the rare-earth-element record of mantle melting for cooling of the Tertiary Iceland plume. *Nature* **395**, 591–594.

Wessel, P. & Kroenke, L. W. (2000). Ontong Java plateau and Late Neogene changes in Pacific plate motion. *Journal of Geophysical Research* **105**, 28, 255–28, 277, doi:10.1029/2000JB900290.

Wessel, P. & Kroenke, L. W. (2007). Reconciling Late Neogene Pacific absolute and relative plate motion changes. *Geochemistry, Geophysics, Geosystems* **8**, Q08001, doi:10.1029/2007GC001636.

Wessel, P. & Kroenke, L. W. (2009). Observations of geometry and ages constrain relative motion of Hawaii and Louisville plumes. *Earth and Planetary Science Letters* **284**, 467–472.

White, W. M., Hofmann, A. W. & Puchelt, H. (1987). Isotope geochemistry of Pacific midocean ridge basalt. *Journal of Geophysical Research* **92**, 4881–4893.

Wilder, D. T. (2003). Relative motion history of the Pacific–Nazca (Farallon) plates since 30 million years ago, MSc dissertation, College of Marine Science, University of South Florida, St. Petersburg, p. 105.

Woods, M. T. & Okal, E. A. (1994). The structure of the Nazca Ridge and Sala y Gomez Seamount Chain from the dispersion of Rayleigh waves. *Geophysical Journal International* **117**, 205–222.

Workman, R. K. & Hart, S. R. (2005). Major and trace element composition of the depleted MORB mantle (DMM). *Earth and Planetary Science Letters* **231**, 53–72.

York, D. (1969). Least squares fitting of a straight line with correlated errors. *Earth and Planetary Science Letters* **5**, 320–324.

York, D., Evensen, N. M., Martínez, M. L. & Delgado, J. D. B. (2004). Unified equations for the slope, intercept, and standard errors of the best straight line. *American Journal of Physics* **72**, 367–375.